Submitted to Electrochimica Acta

LBL-5724
Preprint c. 1

# RECENT ADVANCES IN SOME EXPERIMENTAL OPTICAL METHODS

Rolf H. Muller

November 1976

Prepared for the U. S. Energy Research and Development Administration under Contract W-7405-ENG-48



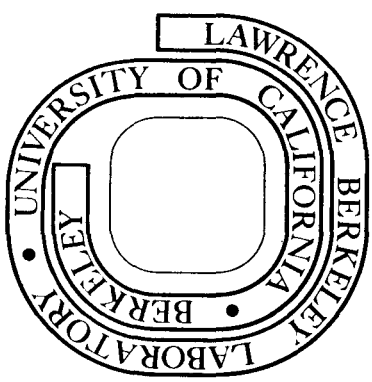

## DISCLAIMER

LBL-5724

# RECENT ADVANCES IN SOME EXPERIMENTAL OPTICAL METHODS

Rolf H. Muller

Materials and Molecular Research Division
Lawrence Berkeley Laboratory
and
Department of Chemical Engineering
University of California, Berkeley, California 94720

## INTRODUCTION

Electrochemistry relies to a large extent on experimental information to advance the understanding of fundamental processes and to expand the range of practical applications. It has long been recognized that the measurement of the classical electrochemical variables, current, potential and charge is often not sufficient for the detailed characterization of electrochemical processes. It may not be as well known that at high current densities, a regime of possible future technical interest, potential is extremely difficult to measure and may be impossible to control.

Many new experimental techniques to augment electrochemical observations have been introduced in recent years. A part of these techniques can be applied simultaneously with electrochemical measurements. Prominent among these *in situ* methods are some of the spectroscopic techniques, more of a dozen of which have now been used for electrochemical studies [1]. Other techniques require the transfer of specimens into special environments, such as vacuum. Many methods borrowed from modern surface science fall into this second *ex situ* category.

In the following, I wish to point out some innovations that we have developed in our laboratory in four optical techniques for the investigation of scientific problems of technical significance. The methods belong to the in situ variety and are interferametry, Doppler velocimetry, ellipsometry and thin film interference. The phenomena under study are mass transport processes and the formation of solid and liquid films.

## INTERFEROMETRY

Optical interferometry for the study of electrochemical transport processes has been used by a number of investigators since Ibl had demonstrated the usefulness of the technique more than twenty years ago [2]. In joint work with C. W. Tobias, we have applied interferometry to larger electrode geometries. We have built a four plate inferometer [3] that uses, as innovations, a dual-emission laser as a light source and an objective-lens placement favorable for high geometrical resolution (Fig. 1).

### Light Deflection in the Boundary Layer

In the course of this work, we found it necessary to investigate the effect of two optical aberrations. The first is light deflection in the boundary layer [4-6]. With a metal deposition boundary layer (Fig. 2), a light beam is deflected away from the electrode. It therefore runs through regions of different concentration and appears

to come from a virtual origin which is different from its real origin at the entrance to the cell. The conventional interpretation of interferograms is based on the straight-line propagation of light; interference fringes are then a direct representation of concentration fields, as shown by the broken curve BF in Fig. 3. If light deflection is taken into account, however, the concentration profile indicated by the solid line A E, which also agrees with what one would expect, is derived. As you see, light deflection can cause serious distortions of interferograms in both coordinate directions. We have derived a complete understanding of light-deflection effects for one-dimensional and some two-dimensional concentration fields.

Reflection from the Electrode Edge

Another problem in the quantitative interpretation of interferograms concerns the location of the interface in the absence of refractive-index variations. We have identified reflection from the edge of the electrode [7] as the principal cause of this problem. Even with the most careful polishing procedures, the electrode edge facing the light beam exhibits a finite radius of curvature (Fig. 4). Reflection from this edge causes a displacement of interference fringes similar to that caused by concentration variation (Fig. 5A), and is more pronounced for a more rounded electrode edge (Fig. 5B). The effect can be almost eliminated for the better electrode (Fig. 5C) or greatly reduced for

the worse electrode (Fig. 5D) by a change in focal plane from the elctrode edge to inside the cell. The extent to which the focus can be changed is limited by diffraction effects that are just beginning to appear in Fig. 5C.

Diffusive Boundary Layers

If all these aberrations are taken into account [6], we find that interfacial concentration, indeed, goes to zero when limiting current conditions are reached [8], as indicated by the rise in potential (Fig. 6). Conventional interferogram interpretation would lead one to postulate a finite interfacial concentration instead. These measurements also just barely suggest a concentration dependence of transport properties: two theoretical curves derived for different concentration dependence of diffusion coefficient and transference number are in better agreement with measurements than expectations based on the Sand equation (dashed line) that assumes constant transport properties.

Convective Boundary Layers

Interferograms obtained with a 1 cm wide and 100 cm long electrode in a flow channel illustrate the decrease in boundary layer thickness with increasing Reynolds Number [9] in the laminar and turbulent regime (Fig. 7). Please note that the electrode shadow is displaced from the true location of the interface, indicated by the origin of the distance coordinate, because of light-deflection effects. The quantitative evaluation of interferograms has shown that

the expected increase in the thickness of the Nernst (effective) mass-transport boundary layer with the 1/3 power of the distance from the leading edge for laminar flow (Fig. 8). A surprising observation was [9] that steady state boundary layers under forced convection are established by an abrupt transition from a growth phase that is the same as in the absence of convection (Fig. 9).

An effective way to decrease boundary layer thickness and, thus, increase current density with channel flow consists in superimposing natural convection on the forced convection [10]. Interferograms of the transient build-up of boundary layers on horizontal electrodes in the absence and presence of natural convection are shown in Fig. 10, top and bottom, respectively [9]. Under the conditions illustrated, the Rayleigh criterion is exceeded after 20 sec and natural convection, that manifests itself by the wavy interference fringes, sets in at the upward-facing cathode. Steady state is reached after 30 seconds. Comparison with the interferogram for the downward-facing cathode, where no natural convection occurs, illustrates the great reduction in effective boundary layer thickness caused by natural convection. The wavy interference fringes result from the superposition of a three-dimensional concentration field and do not necessarily represent adjacent concentration minima and maxima.

Another means of reducing boundary layer thickness is the use of turbulence-inducing flow obstacles at the

electrode surface. The effect of a 0.76 mm high triangular obstacle is shown in Fig. 11, with interferograms of the boundary layer 5 mm upstream from the obstacle, at the obstacle and at three distances downstream from it [9]. It can be seen that the thickness of the boundary layer immediately upstream from the obstacle is greatly reduced, even 25 mm (or 33 times the obstacle height) downstream; it regains its original extent 125 mm downstream. Much smaller effects have been observed with smaller obstacles and lower Reynolds numbers.

## VELOCIMETRY

Complex flow patterns, as illustrated by the superimposed forced and natural convection, are best determined by local velocity measurements. Laser Doppler velocimetry is a new technique to make such measurements [11,12]. This technique is based on observing light scattered from suspended particles and interpreting the difference in frequency between incident and scattered light in terms of the velocity of the particle.

We have built a Doppler velocimeter that can operate in two modes (Fig. 12). In the reference made, a thin light beam is focused in the volume element to be observed. Light scattered from particles moving through this element is collected over a large angle and brought to interference with part of the incident beam. The difference frequency

is a measure of the velocity component along the optical axis. In the differential mode, two incident beams intersect in the probe volume. Here, the difference frequency is contained in the scattered light and is a measure of the velocity component in the plane of the two incident beams. If the beam splitter is rotated by 90°, all three velocity components can be determined sequentially.

Special optical problems arise from the need to observe a very small volume element close to the electrode surface, which makes it necessary to work with backscattered rather than forward scattered light. We also are taking the effect of light bending in the boundary layer into account.

## ELLIPSOMETRY

Ellipsometry is presently in a state of rapid development. In this technique, polarized light is reflected from the electrode and changes in the state of polarization are interpreted in terms of properties of the reflecting surface. Two parameters are normally measured [13], the difference in phase and the ratio of amplitudes of two orthogonal components, one in the plane of incidence, the other normal to it. With some instruments, changes in reflectivity can also be measured as a third parameter [14].

### Automatic Ellipsometers

Automatic ellipsometers of different designs have been built over the last few years to provide more rapid

response and greater sensitivity than what is possible with manual operation. Automatic instruments can be divided into compensating types, in which extinction is achieved by restoring linear polarization, and non-compensating types, in which elliptic polarization states are determined from light intensity measurements. The best performances of both types of instruments [15] are at present quite similar. Slew rates are 3000-6000°/sec and resolutions of the order of 0.001°, which translates to a capability to follow film growth up to a few μm/sec and to detect less than 1% of a monomolecular coverage. Non-compensating ellipsometers are more easily adaptable to wavelength scanning.

Properties of Surface Layers

Ellipsometer measurements are unusually sensitive to the presence and properties of surface layers on electrodes, that can be observed while immersed in any optically transparent electrolyte. The anodic formation of a cuprous oxide layer on copper under different mass transport conditions may serve as an illustration of this capability (Fig. 13). Starting at the bare surface, represented by the circle at the right, ellipsometer measurements $\psi$ and $\Delta$ shown by the solid line can be interpreted by use of the optical properties of compact cuprous oxide, while the broken line requires the assumption of properties characteristic of porous oxide. Scanning electron micrographs of layers formed under both conditions, shown in Fig. 14, have confirmed the compact and porous nature of the two films [16].

Boundary Layer Effects

In the course of adapting ellipsometry to the observation of high-rate electrode processes, we have investigated the effect of mass-transport boundary layers on the ellipsometry of electrode surfaces [17], since boundary layers are unavoidably associated with electrode processes which proceed at finite current densities. The optical effect of different refractive-index profiles in the boundary layer (Fig. 15) has been analyzed theoretically. This work has shown that homogeneous layers, such as the one indicated by the dotted line, do not provide good optical models and inhomogeneous films, with continuously variable refractive index, have to be used instead. The exact nature of the inhomogeneous films is, however, surprisingly unimportant for their optical effect [17].

Inhomogeneous layers, such as the linear or parabolic profiles shown in Fig. 15 are computationally treated as a stack of a large number of homogeneous layers. At each interface between successive layers light refraction and relection takes place (Fig. 16). For most electrochemical boundary layers, refractive index gradients are small enough to cause reflection from within the boundary layer to be negligible. The main optical effect of the boundary layer is then a change in the angle of incidence $\phi_i$ at the electrode surface from the angle $\phi_b$ expected in the absence of a boundary layer. This effect is responsible for the

otherwise unexpected independence of ellipsometer measurements on boundary layer thickness for thicknesses of normal electrochemical interest (above 1 μm), predicted by computation (Fig. 17) and confirmed by experiment [16,17]. Boundary layers associated with metal deposition result in opposite effects from those of metal dissolution. In both cases, the magnitude of the effect depends strongly on the optical constants of the electrode material.

Measurement of Interfacial Concentration

It follows that ellipsometry can be considered a new technique for the measurement of interfacial concentration at electrodes. We have experimentally tested this assertion by the time-honored convectionless deposition of copper at constant current. The electrolysis cell and some components of our automatic ellipsometer are shown in Fig. 18. Light propagates from left to right and is reflected from the downward-facing cathode. The expected inverse square root behavior of the interfacial concentration is confirmed by the measurements shown in Fig. 19 [16]. Ellipsometry is of particular interest for boundary layers that are too thin for observation by interferometry (smaller than about 30 μm).

A very recent application of ellipsometry for measuring interfacial refractive index is the determination of the concentration of supporting electrolyte at an electrode under limiting current conditions. Results given in Fig. 20 for sulfuric acid and copper sulfate illustrate that the

accumulation of sulfuric acid at the electrode surface can reach 20% of the bulk concentration [16]. These data are close to early estimates by Tobias and Eisenberg [18], and are bracketed by recent computations by Newman [19] for complete and incomplete dissociation of the acid.

Metal Dissolution

An example of anodic film formation in which boundary layer effects are prominent is seen with Zn in KOH [16]. The two measured ellipsometer parameters $\psi$ and $\Delta$, starting from those for the bare Zn surface at the upper right of Fig. 21, first indicate roughening of the metal surface. Dissolved reaction products can then be observed to accumulate in the boundary layer. After saturation concentration is reached, the growth of a solid, passivating film sets in. The observed film growth reasonably follows computed points indicated for different film thickness.

## THIN FILM INTERFERENCE

Although interference colors have been observed for a long time and have been scrutinized by modern means [20], their use for the quantitative determination of the thickness of transparent liquid or solid films on electrodes has required our introduction of further optical considerations, which I wish to outline briefly. Two factors, namely phase change in reflection and color purity, as affected by angle of incidence, have resulted in the derivation of generalized

interference color series. By use of these series, local film thickness in the range of 0.1 - 2 μm can be determined over extended surfaces by convenient photographic or visual observation [21].

Phase Change in Reflection

With no phase change in reflection, a maximum in luminance or brightness (represented by the tristimulus value Y) of interference colors is obtained with films of vanishing thickness (Fig. 22 lower curves). The first luminance minimum occurs at half an average wavelength optical path in the films. Subsequent minima and maxima are less pronounced; their size and shape depend on the reflection coefficient r of the interfaces. For 180° phase change due to reflection, destructive interference occurs with vanishing film thickness (upper curves in Fig. 22). Transparent films on metal surfaces exhibit phase changes that are different from 0° or 180°. Typically, phase changes with p-polarization are represented in the upper half of the diagram, s-polarization in the lower half. With increasing film thickness, interference therefore starts between complete constructive or destructive interference. The phase change due to reflection primarily depends on the polarization and the optical constants of the metal substrate. Figure 23 illustrates that the phase change can assume widely varying values for different electrode materials. (The value shown for the film-substrate interface has to be subtracted from the phase

change for the film-air interface, which is 180° for p-polarization above Brewster's angle, in order to obtain the total phase change due to reflection.)

Purity of Interference Colors

Transparent films on a metal substrate typically reflect more light from the bottom (metal) interface than from the top near normal incidence (Fig. 24a). The resulting interference contrast, or the purity (saturation) of interference colors, is therefore poor. Near grazing incidence, on the other hand, most of the light is reflected from the top surface, and interference likewise is poor (Fig. 24c). At an intermediate angle of incidence, which we call the optimum angle, the two interfering waves are of equal amplitude, so they completely cancel each other under conditions of destructive interference. We have introduced the colorimetric quantity of color purity to define the optimum angle of incidence for the observation of most saturated thin film interference colors.

Colorimetry

The tristimulus theory of color preception [22] has been used for the computation of interference colors. In the CIE system, 3 primary colors are defined by the distribution coefficients $\bar{x}$, $\bar{y}$ and $\bar{z}$ (Fig. 25). Products of these distribution coefficients with the spectral energy distribution are integrated and result in three tristimulus values that can be normalized and shown in an x, y chromaticity diagram (Fig. 26). Any point inside the horseshoe-shaped diagram

represents a color that lies between the spectrally pure colors shown by wavelength and spectral name on the outline of the diagram and the white (or achromatic) region inside it. The figure also shows the color (hue) names that have been assigned to segments of the chromaticity diagram for the description of computed interference color series.

Color purity is defined as the relative separation of a color locus from the white point and the spectral color of the same dominant wavelength (along a straight line through achromatic point and color locus, Fig. 27).

Optimum Angle of Incidence

For p-polarization, color purity is zero at Brewster's angle $\phi_p$ and goes through a sharp maximum at the optimum angle of incidence (Fig. 28). The maximum is less peaked for the higher interference orders.

The optimum angle of incidence depends primarily on the optical constants of the substrate. Values between 70° and 90° are typical (Fig. 29).

The sequence of interference colors for a film of increasing thickness can be represented as a curve in the chromaticity diagram. This curve is farthest from the white point at the optimum angle (Fig. 30).

Generalized Interference Color Series

Charts of generalized interference color series have been constructed from chromaticity curves computed for the optimum angle of incidence with different phase changes due

to reflection and given reflection coefficients. An example is shown in Fig. 31. For any phase change, a color series with increasing film thickness (shown as optical path in the film) can be read along a horizontal line on the chart. One can see that with a phase change of 30°, typical for s-polarization, interference colors change rapidly for very thin films (0.2 to 0.3 μm optical path, corresponding to 0.1 - 0.15 μm film thickness). With p-polarization, on the other hand, for which the phase change may be 230°, color changes at low thickness are weak and the first thickness-sensitive strong color change occurs around 0.5 μm optical path. The chart also illustrates the non-repetitive nature of interference colors, which is an advantage over monochromatic interference.

Equipment

The fact that one polarization is sensitive at thickness intervals where the other is not sensitive has been our reason for using both polarizations simultaneously in experiments (Fig. 32). Two collimators provide s and p polarized parallel illuminating beams that are directed on the specimen at the optimum angle of incidence. The two reflections are collected by a minor system and recorded with a camera. This equipment has been used for the observation of tapered cryolyte films on substrates of intermediate and high reflection coefficient (Cr and Al) under varying angles of incidence.

Experimental interference colors have been compared with computer-drawn graphs of colorimetric computations in a movie film.

## OUTLOOK

I have tried to present some newly-developed aspects of optical experimental methods. Most of them need to be fully exploited yet. Each of these techniques, in addition to its special capabilities, has, of course, its own limitations. I believe, however, that new combinations of experimental approaches can be found that contribute to the advancement of the physical and chemical understanding of electrochemical processes in ways not previously possible.

## ACKNOWLEDGEMENT

This work was conducted under the auspices of the U.S. Energy Research and Development Administration.

REFERENCES

1. Symposium on Spectroscopic Methods in Electrochemical Studies, Electrochemical Society Meeting, May 2-7, 1976, Washington, D. C. Extended Abstracts No. 342-369, Electrochemical Society, Princeton, N. J., 08540, 1967.

2. N. Ibl, Y. Barrada and G. Trümpler, Helv, Chim, Acta 37, 583 (1954). N. Ibl and R. Müller, Ber. Bunseges 59, 671 (1955).

3. K. W. Beach, R. H. Muller and C. W. Tobias, Rev. Sci. Instr. 40, 1248 (1969).

4. K. W. Beach, R. H. Muller and C. W. Tobias, J. Opt. Soc. Am. 63, 559 (1973); R. H. Muller, Double Beam Interferometry for Electrochemical Studies, in Advances in Electrochemistry and Electrochemical Engineering, Vol. 9, Wiley-Interscience, New York, 1973.

5. F. R. McLarnon, R. H. Muller and C. W. Tobias, J. Electrochem. Soc. 122, 59 (1975); 1636 (1975) [Discussion].

6. F. R. McLarnon, R. H. Muller and C. W. Tobias, J. Opt. Soc. Am. 65, 1011 (1975).

7. F. R. McLarnon, R. H. Muller and C. W. Tobias, Appl. Opt. 14, 2468 (1975).

8. F. R. McLarnon, R. H. Muller and C. W. Tobias, Electrochim. Acta 21, 101 (1976).

9. F. R. McLarnon, R. H. Muller and C. W. Tobias, in preparation; F. R. McLarnon, Ph.D., Thesis, Department of Chemical Engineering, University of California, Berkeley, December, 1974.

10. C. W. Tobias and R. G. Hickman, Z. Phys. Chem. 229, 145 (1965).

11. Y. Yeh and H. Z. Cummins, Appl. Phys. Lett. 4, 176 (1964).

12. R. J. Goldstein and W. F. Hagen, Phys. Fluids 10, 1349 (1967).

13. R. H. Muller, Principles of Ellipsometry, in Advances in Electrochemistry and Electrochemical Engineering, Vol. 9, Wiley-Interscience, New York 1973.

14. J. Horkans, B. D. Cahan and E. Yeager, J. Electrochem. Soc. 122, 1585 (1975).

15. R. H. Muller, Surface Sci. 56, 19 (1976).

16. C. G. Smith and R. H. Muller, in preparation; C. G. Smith, M.S. Thesis, Department of Chemical Engineering, University of California, Berkeley, December 1975.

17. R. H. Muller and C. G. Smith, Surface Sci. 56, 440 (1976).

18. C. R. Wilke, M. Eisenberg and C. W. Tobias, J. Electrochem. Soc. 100, 513 (1953).

19. L. Hsueh and J. Newman, Ind. Eng. Chem. Fund. 10, 615 (1971); J. R. Selman and J. Newman, J. Electrochem. Soc. 118, 1070 (1971).

20. H. Kubota, Interference Color, in Progress in Optics, Vol. 1, E. Wolf, ed., North-Holland, Amsterdam 1961.

21. R. H. Muller and M. L. Sand, in preparation; M. L. Sand, M.S. Thesis, Department of Chemical Engineering, University of California, Berkeley, June 1975.

22. W. D. Wright, The Measurement of Colour, Van Nostrand, New York 1969, 4th ed.

FIGURE CAPTIONS

Fig. 1 Four plate interferometer with dual-emission laser light source. The interferometer travels on a lathe bed carriage along the electrodes contained inside the flow channel that extends in the direction away from the observer [9].

Fig. 2 Light deflection in a metal deposition boundary layer. Imaging optics of interferometer focused on scribe marks in the real plane of focus. Virtual location of marks and virtual origin of deflected beam in virtual plane of focus. Beyond the equi-phase circle, centered at the virtual beam origin, the imaging optics introduce no phase difference between deflected and undeflected beams.

Fig. 3 Interferogram of convectionless mass-transfer boundary layer with interpretation in the conventional way, BF, and under consideration of light-deflection, AE. Galvanostatic depositon of Cu at 10 $mA/cm^2$ from 0.1 M $CuSO_4$, 10 s after begin of deposition [5].

Fig. 4 Microprofile of electrode cross-section. Light propagation in the interferometer from left to right; reflection occurs at the slightly rounded electrode edge at the left [9].

Fig. 5 Effect of light reflection from electrode edge on interferograms in the absence of concentration variations. A, C best square edge, B, D deliberately

round edge. A, B focus at electrode edge (inside face of cell window facing light source); C, D focus 0.5 mm inside cell [7].

Fig. 6 Interferometrically determined transient interfacial concentration (●) and cell voltage in convectionless galvanostatic Cu deposition from 0.1 M $CuSO_4$ at 10 mA/cm$^2$ [8]. Theoretical expectations for:

--- $D = 5.41 \times 10^{-6}$ cm$^2$ sec$^{-1}$,

$t_+ = 0.364$ (Sand eq.).

—— $D = 5.41\ (1 - 0.869C) \times 10^{-6}$,

$t_+ = 0.403 - 0.387C$.

-·- $D = 5.75\ (1 - 1.41\ C) \times 10^{-6}$,

$t_+ = 0.403 - 0.387C$.

Fig. 7 Interferometric observation of boundary layers in a flow channel at different electrolyte velocities. Observation 50 cm downstream from leading edge. Electrodes 1 cm wide and 100 cm long; electrode separation 2.54 cm [9].

Fig. 8 Nernst boundary layer thickness $\delta_N$ derived from interferograms for two laminar flow velocities as a function of distance z from the leading edge. Flow channel as in Fig. 7. 0 - 1.5 mA/cm$^2$ at Re 590, 2.5 mA/cm$^2$ at Re 1500; ∇ - 3 mA/cm$^2$ at Re 590, 5 mA/cm$^2$ at Re 1500.

—— computed, --- uncertainty caused by ± 10% variation in diffusion coefficient [9].

Fig. 9 Transient interfacial concentration for laminar flow, derived from interferograms. Flow channel as in Fig. 7.

—— Asymptotic solution to the convective diffusion equation, --- effect of ± 10% variation in diffusion coefficient [9].

Fig. 10 Boundary layer growth on a downward facing cathode with pure forced convection (top) and on an upward facing cathode with superimposed forced and natural convection (bottom). Interferograms obtained with flow channel as in Fig. 7, Re = 1000, z = 10 cm, 10 $mA/cm^2$ [9].

Fig. 11 Effect of cylindrical flow obstacle of triangular cross-section, 0.76 mm high, attached to the electrode, on boundary layer in Cu deposition. Flow channel as in Fig. 7. Interferometer observation at different distances z from the leading edge. Re 1500, 2.5 $mA/cm^2$.

Fig. 12 Laser Doppler velocimeter for the determination of velocity distributions in boundary layers. Velocity component along optical axis determined in the reference mode; velocity component in the plane of the two intersecting incident beams determined in the differential mode.

Fig. 13 Growth of $Cu_2O$ on Cu in 1 M $NaClO_3$. Observed ellipsometer parameters, relative phase $\Delta$ and relative amplitude $\psi$ for compact and porous oxide formed under different transport conditions [16].

Fig. 14 Scanning electrom micrographs of compact and porour anodic films resulting from the dissolution of Cu in 1 M $NaClO_3$ under different transport conditions.

(a) Re 2310, 240 $mA/cm^2$, 10s;

(b) Re 3060, 407 $mA/cm^2$, 5.9s [16].

Fig. 15 Boundary layer models for ellipsometry. Different refractive index profiles to describe a 10 $\mu$ thick boundary layer with a concentration difference of 0.1 M $CuSO_4$ between interface and bulk solution [16].

Fig. 16 Computation of boundary layer effect in ellipsometry. Representation of inhomogeneous boundary layer by multiple homogeneous films with reflection and refraction at interfaces between them. Angle of incidence $\phi_i$ at the electrode different from angle of incidence $\phi_b$ on the boundary layer [16].

Fig. 17 Effect of metal dissolution boundary layers on ellipsometer parameter $\Delta$. Dissolution of Cu (n = 0.94 - 2.33i) into $CuSO_4$; concentration difference between bulk and interface indicated along curves, computation for parabolic concentration profiles [16].

Fig. 18 Ellipsometry of horizontal, downward-facing electrode. Components from left to right, carrier for quarter-wave compensator, iris diaphragm, electrochemical cell, analyzer Faraday cell.

Fig. 19 Determination of interfacial concentration by ellipsometry. Convectionless deposition of Cu from 0.2 M $CuSO_4$ at different current densities.

—— Sand eq. with $D = 5 \times 10^{-6}$ $cm^2 s^{-1}$,

$t_+ = 0.385$ [16].

Fig. 20 Accumulation of supporting electrolyte at interface determined by ellipsometry. Convectionless Cu deposition from different $CuSO_4$-$H_2SO_4$ compositions at limiting current [16].

Fig. 21 Ellipsometry of anodic film formation. Zn in 0.5 M KOH. Dominant optical effects in succession: surface roughening, build-up of boundary layer and formation of solid film [16].

Fig. 22 White light interference in transparent films. Relative luminance (tristimulus value Y) with increasing optical path length in film (film thickness) for different amplitude reflection coefficients r. Upper curves - phase change due to reflection 180°, lower curves - 0°. ····· Locus of liminance minima, --- locus of luminance maxima

as a function of phase change due to reflection and optical path length in the film [21].

Fig. 23 Phase change and amplitude reflection coefficient for reflection from substrate-film interface. Refractive index of substrate n - ik, of film $n_o$. Angle of incidence on substrate 45°, p-polarization. Locus of representative metals shown for a film of refractive index 1.35.

Fig. 24 Angle of incidence and color purity of thin film interference colors.

(a) Small angle of incidence: reflection higher from bottom of film, resulting in low color purity.

(b) Optimum angle of incidence: reflection from both film interfaces equal, high color purity.

(c) Large angle of incidence: reflection higher from top of film, low color purity.

Fig. 25 Relative intensities of the 1931 C.I.E. primary colors x, y and z and energy distribution of standard tungsten source A used for present colorimetric computations [21].

Fig. 26 C.I.E. 1931 chromaticity diagram. Spectral colors on periphery indicated by names and wavelengths in nm. Ellipse indicating white region for tungsten

source A shown 5 times enlarged. Dashed lines define condensed list of hue names used in present computations [21].

Fig. 27 Definition of color purity in the chromaticity diagram [21].

Fig. 28 Variation of color purity with angle of incidence. Transparent film (n = 1.35) on Pt surface (n = 2.07 - 4.40i), red interference color of dominant complimentary wavelength 506.4 nm, p-polarization.

Fig. 29 Optimum angle of incidence for the observation of thin film interference. Transparent film (n = 1.35) on substrates of optical constants n - ik, p-polarization [21].

Fig. 30 Chromaticity diagram for first-order interference color series. Angle of incidence: 0 - 89°. Optical path in film 0 - 325 nm (corresponds to film thickness 0 - 178 nm at optimum angle). Locus of interference colors at optimum angle of incidence (85°) farthest from the white point (greatest color purity) [21].

Fig. 31 Generalized chart of thin film interference color series for transparent films with arbitrary phase change due to reflection. Amplitude reflection coefficient at both interfaces 0.6, color names as defined in Fig. 26:

B - blue, BG - blue green, G - green,

O - orange, P - purple, R - Red,

W - white, Y - yellow [21].

Fig. 32 Optical bench for observation of thin films on electrodes by white light interference. Light propagation from lower left to upper right. Parallel beams of s and p polarized light are reflected from the specimen surface and recorded by the camera. Fiber optic probes can sample the beams before and after reflection for spectroscopic analysis.

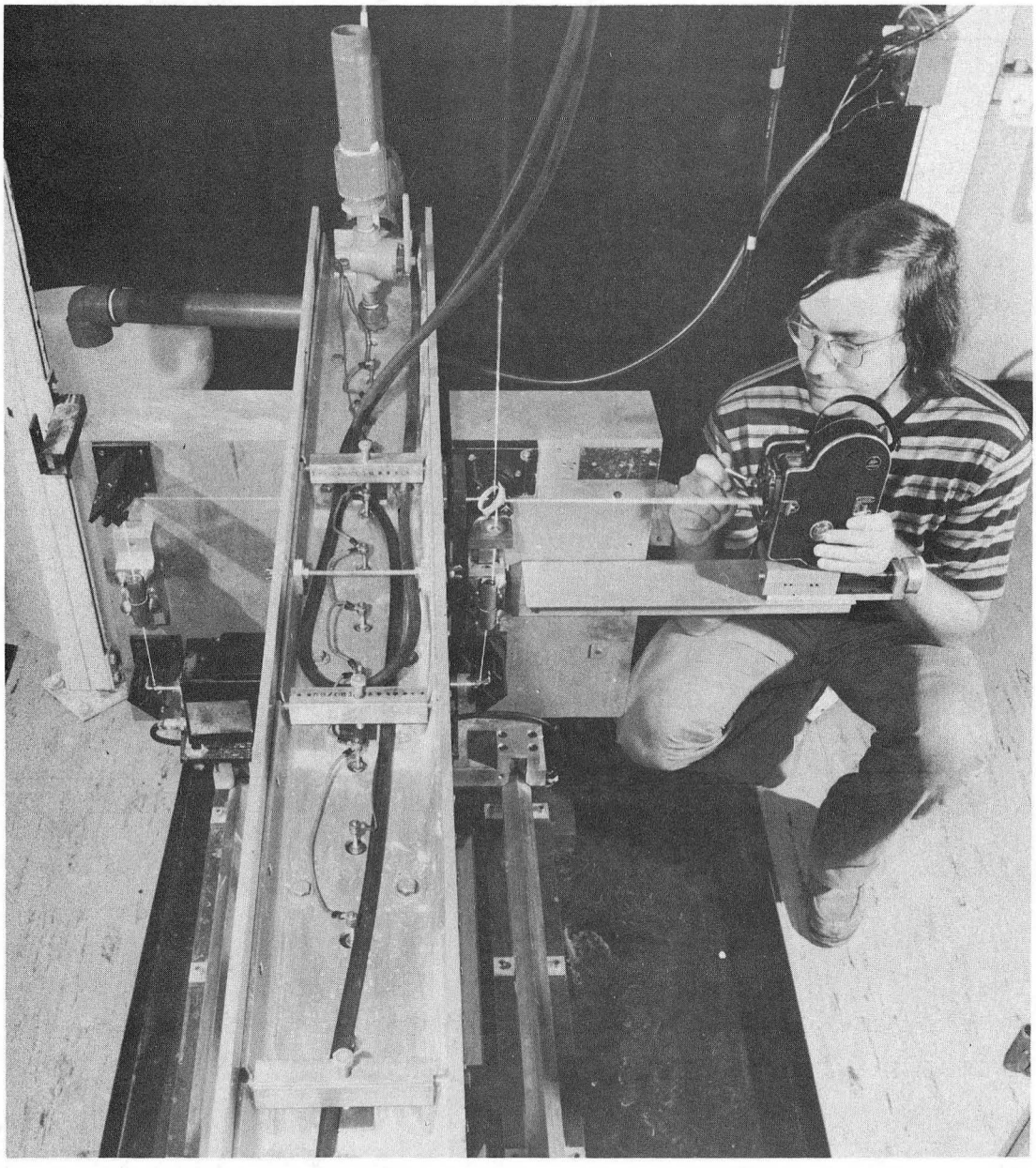

XBB 7410-7137

Fig. 1

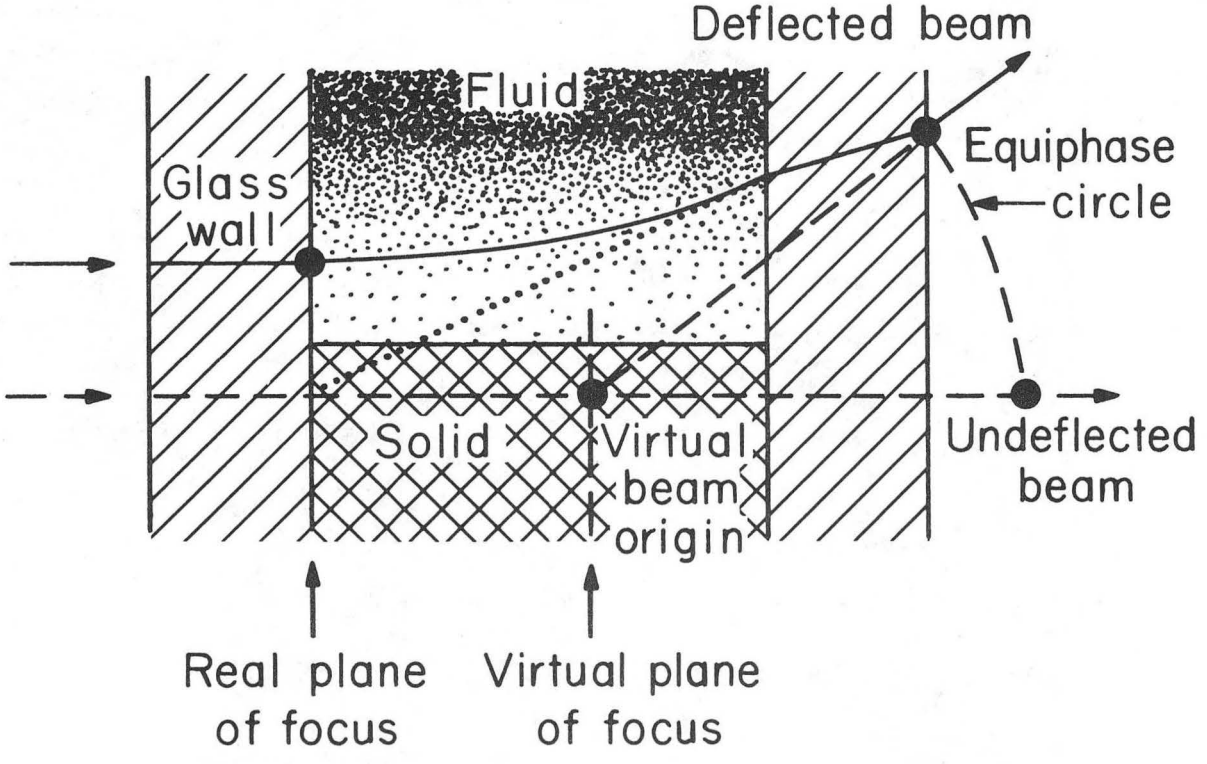


XBL 7410-4372A

Fig. 2

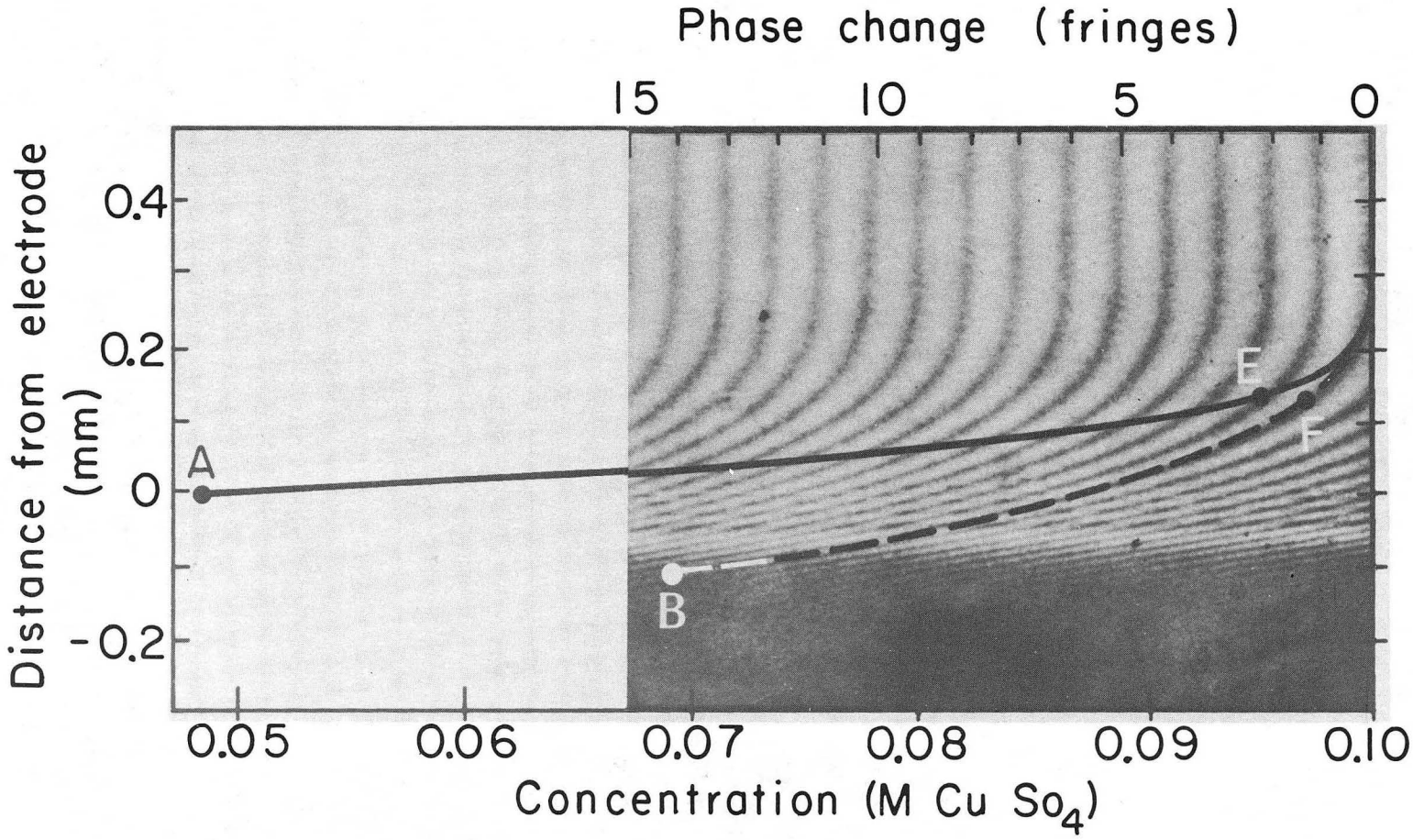


XBB 7311-6546

Fig. 3

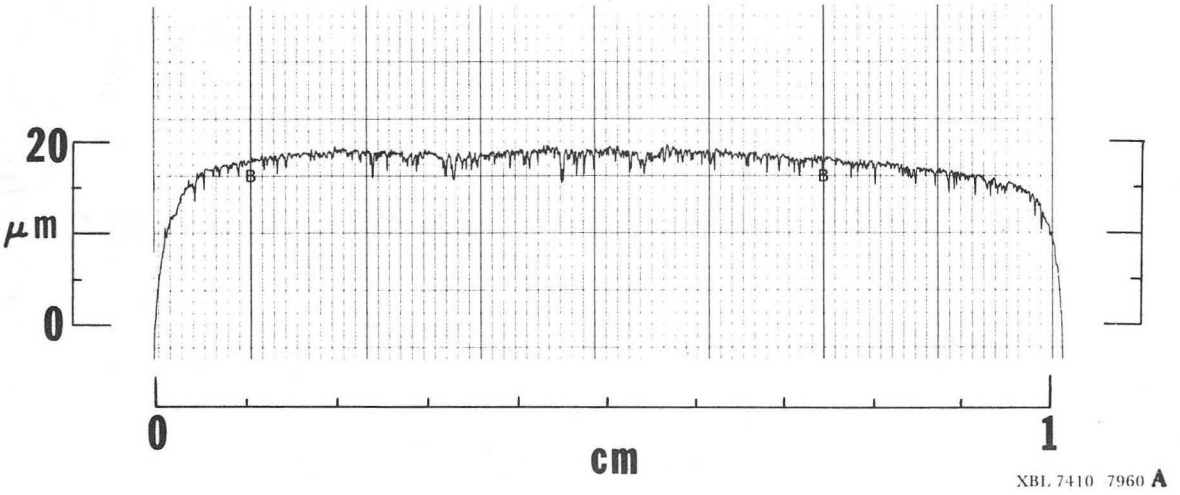


Fig. 4

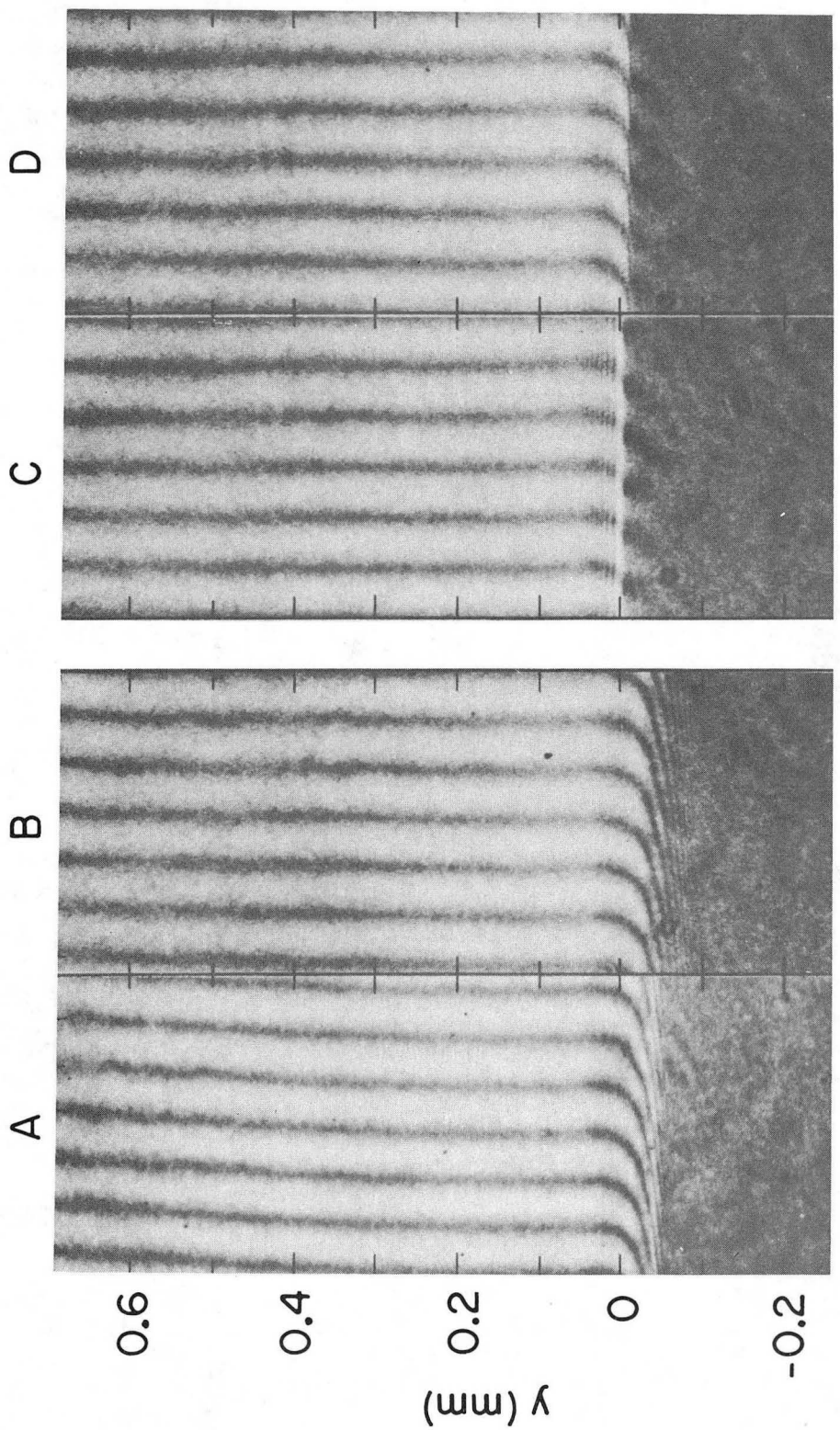


Fig. 5

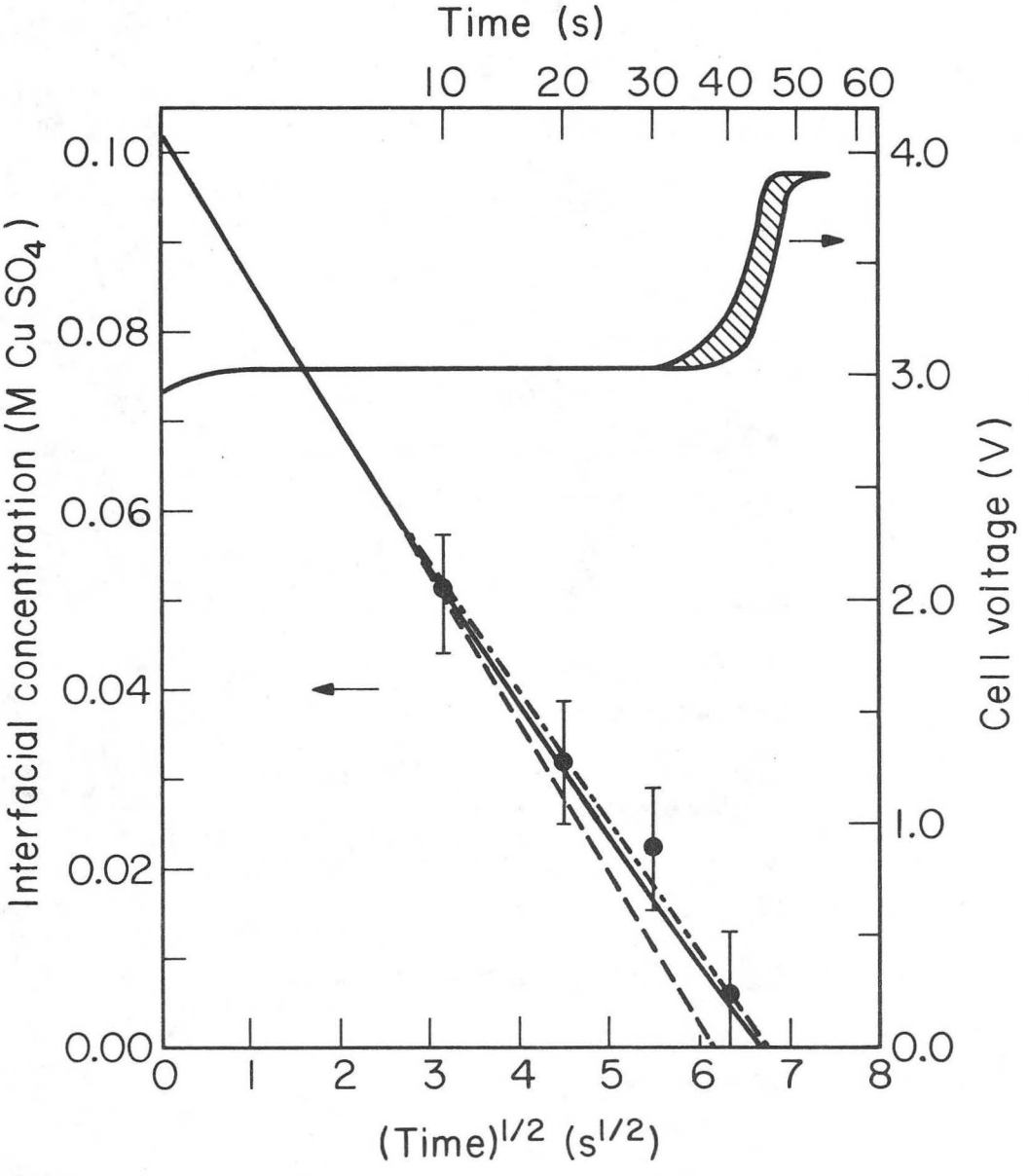


XBL 7410-4371A

Fig. 6

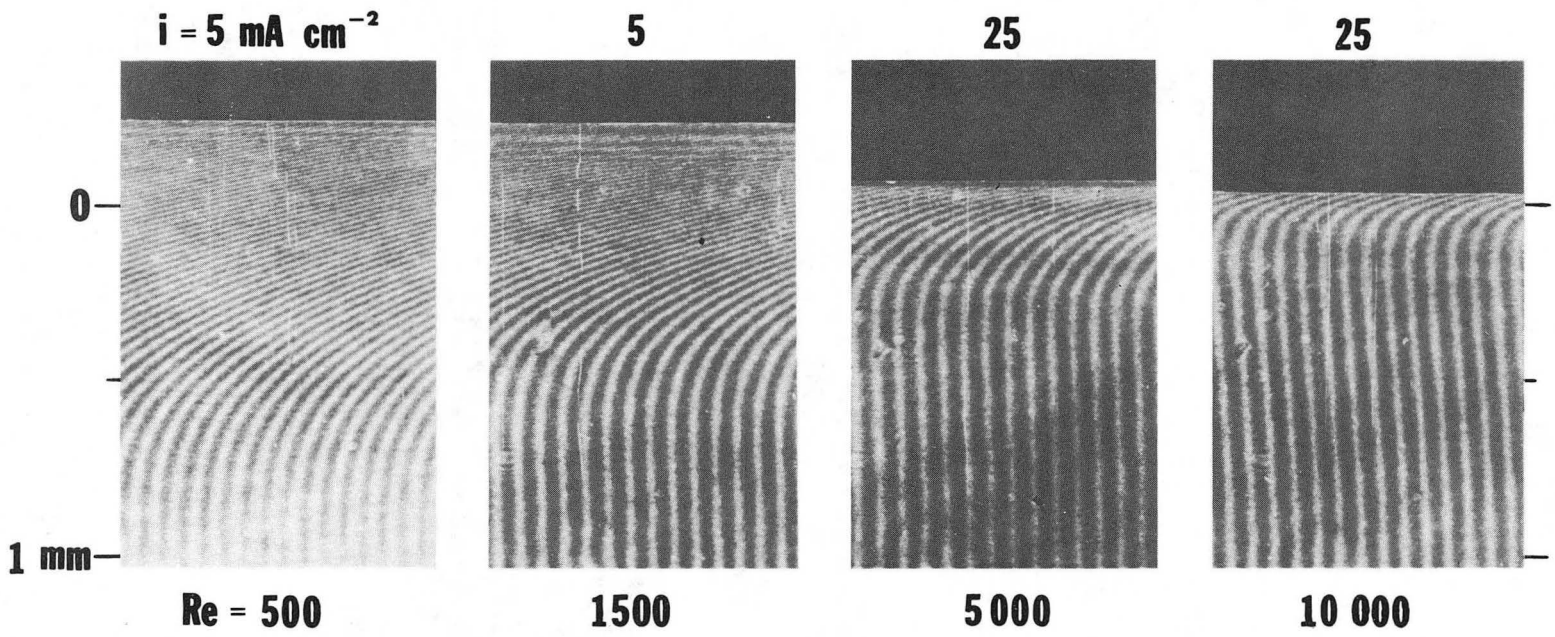


Fig. 7

XBB 748-5798A

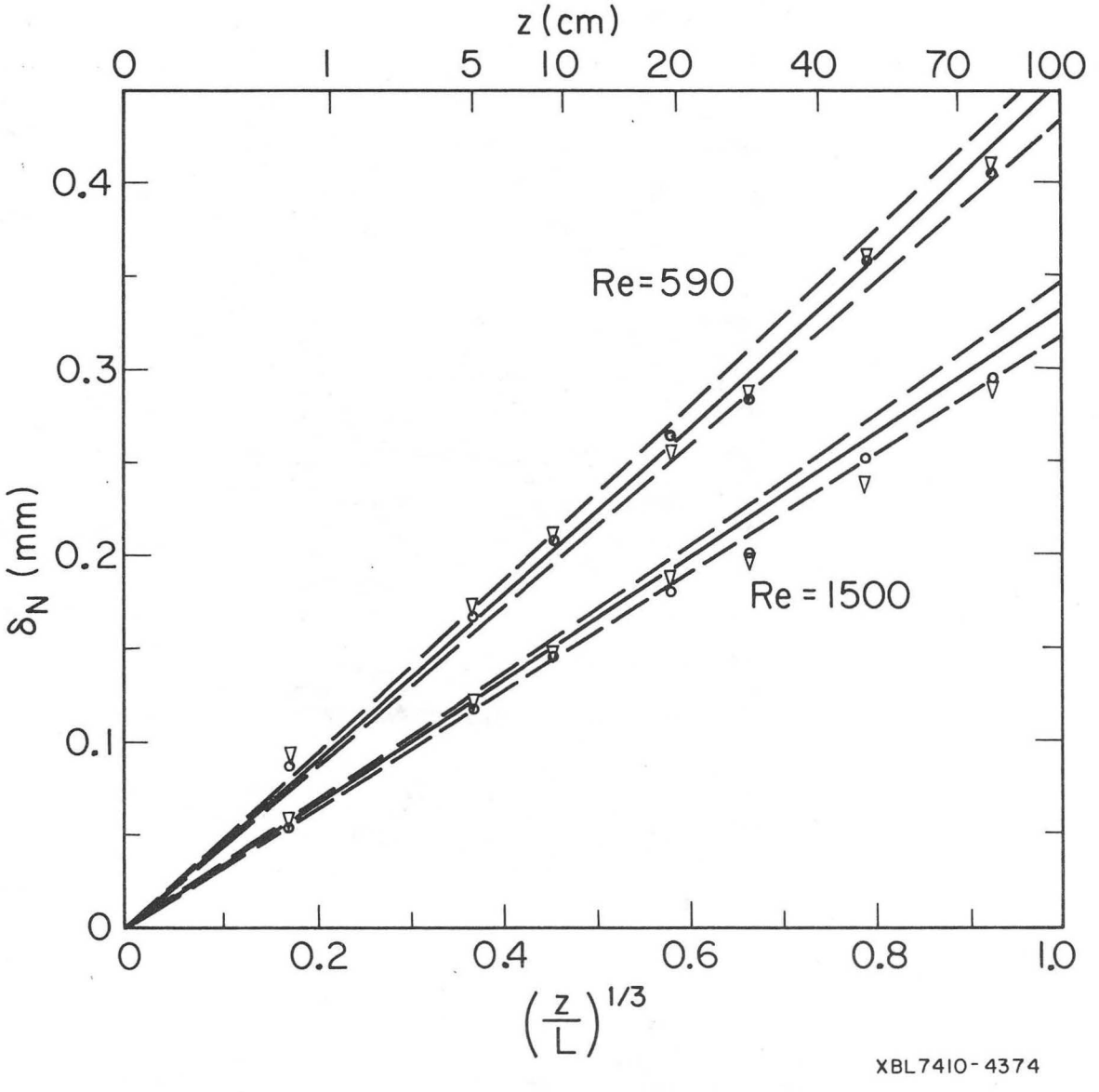
z (cm)
0
1
5
10
20
40
70
100
0.4
0.3
0.2
0.1
0
Re=590
Re = 1500
$\delta_N$ (mm)
0
0.2
0.4
0.6
0.8
1.0
$\left(\frac{z}{L}\right)^{1/3}$
XBL7410-4374

Fig. 8

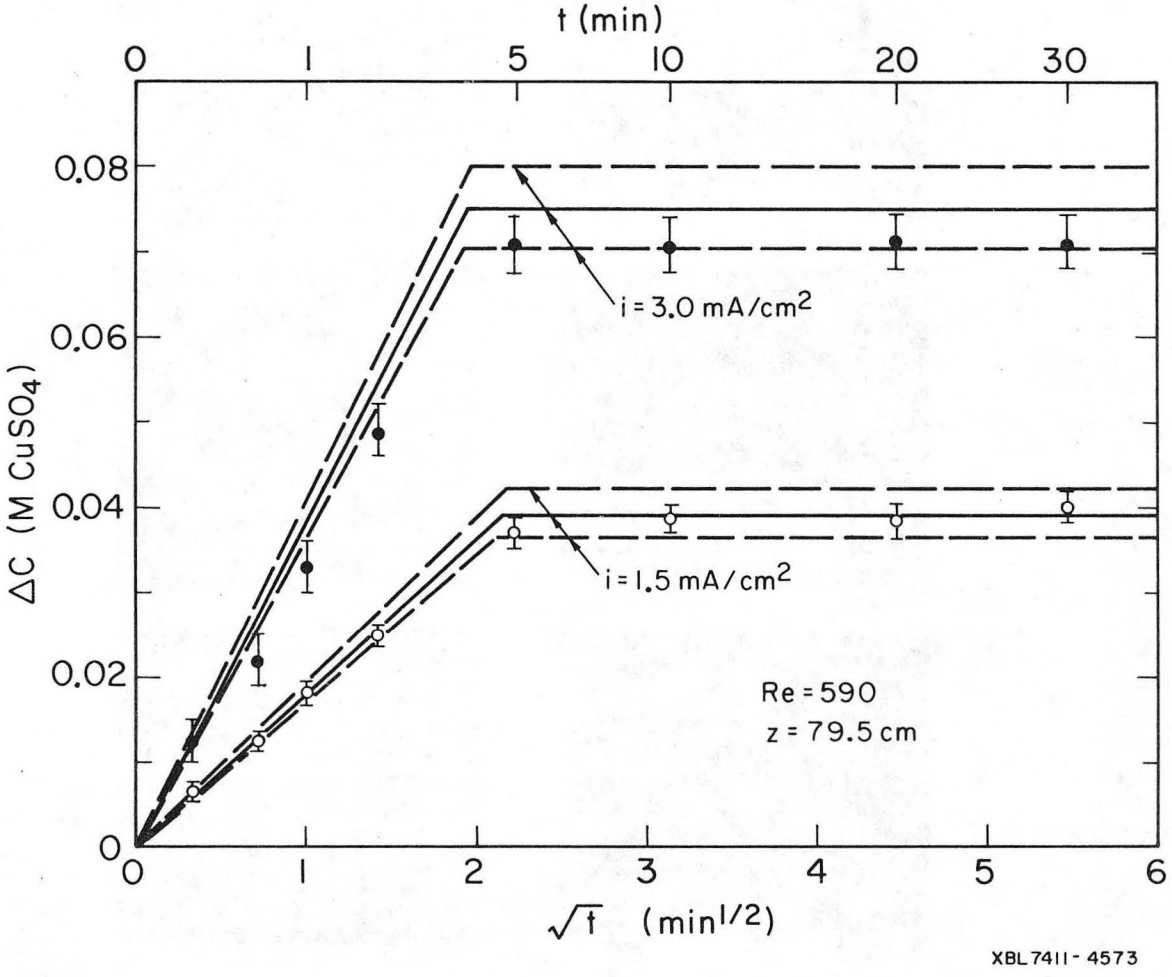


Fig. 9

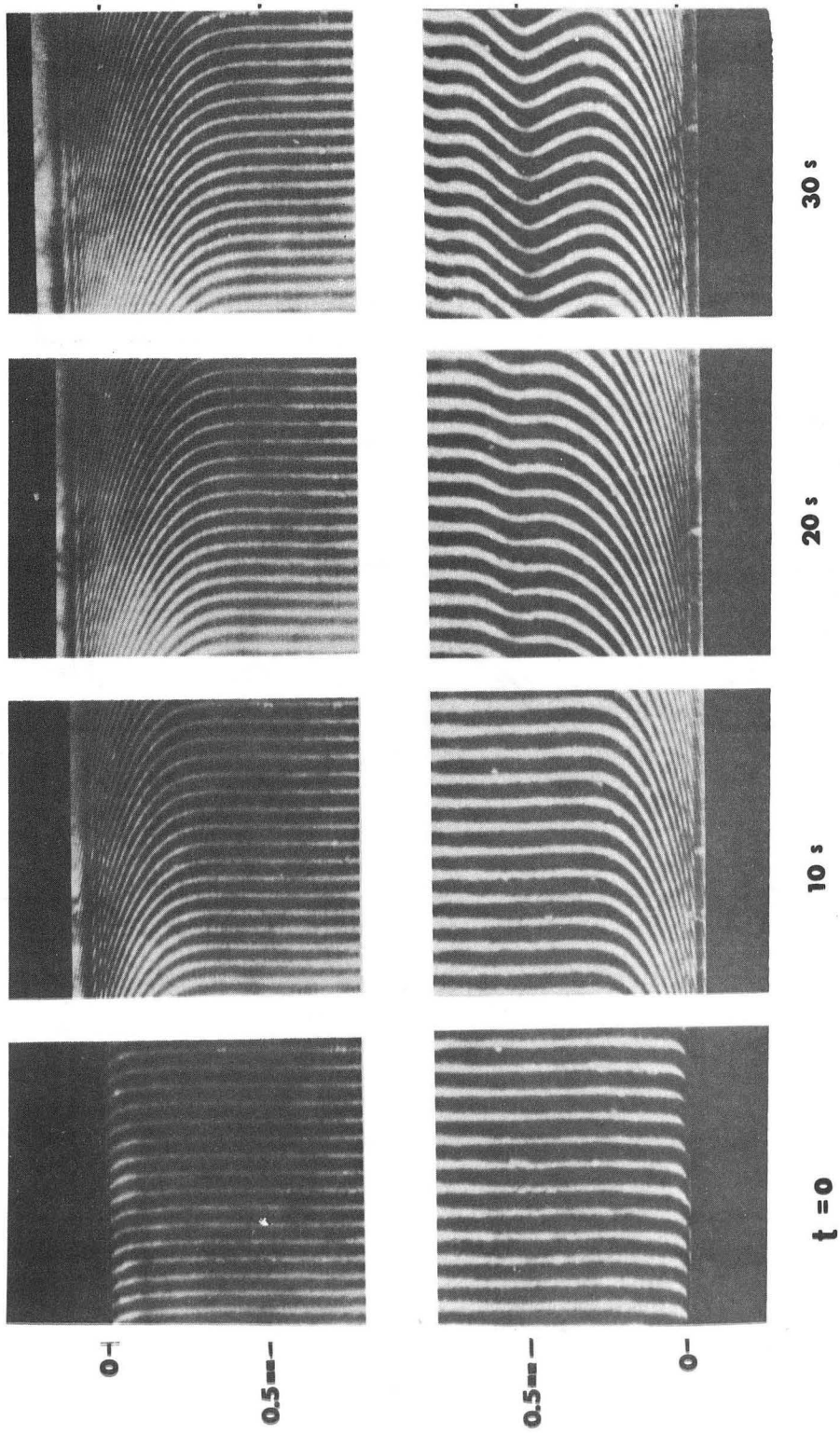


Fig. 10.

XBB 748-5799

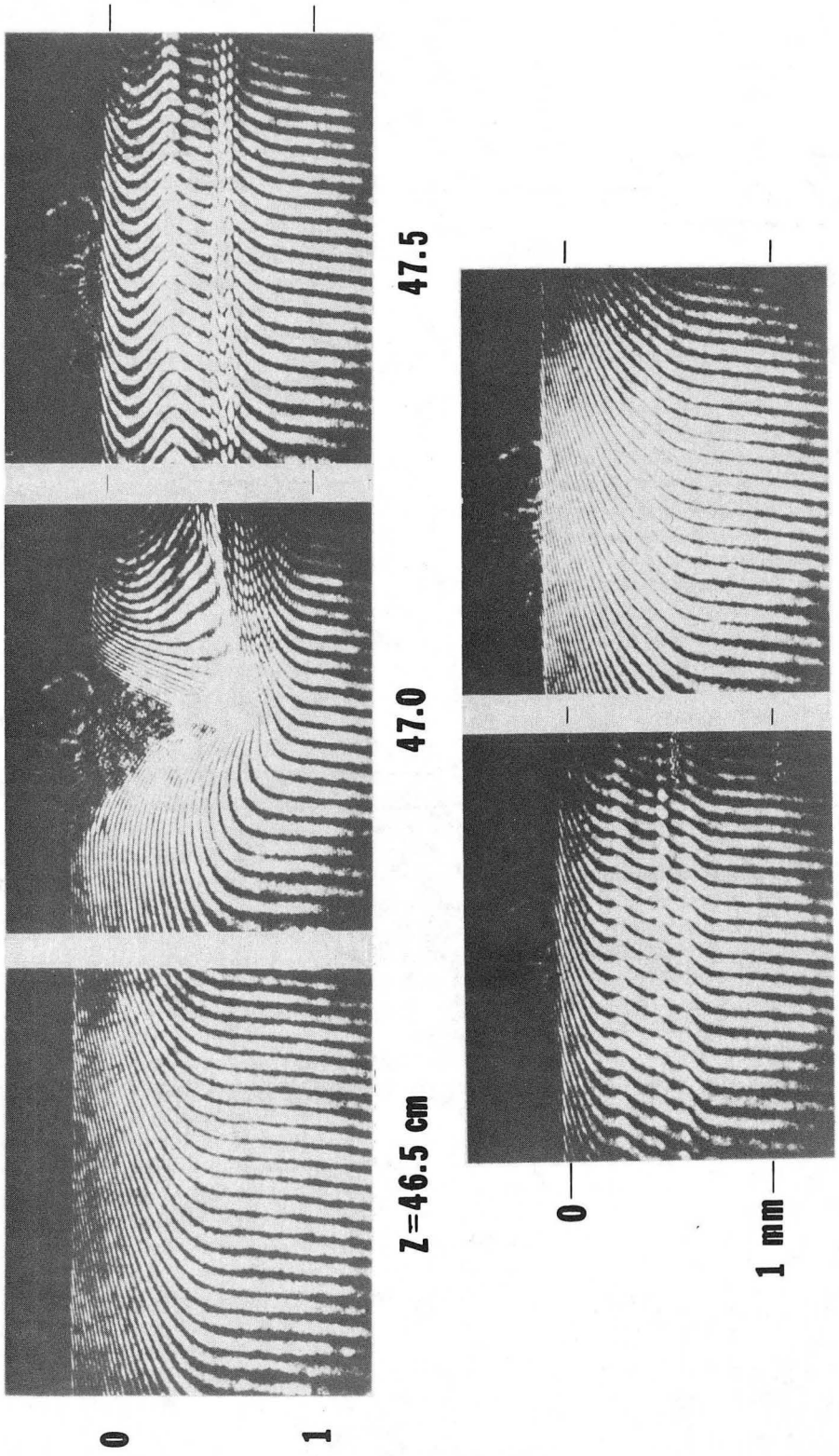


XBB 7411-8126A

Fig. 11

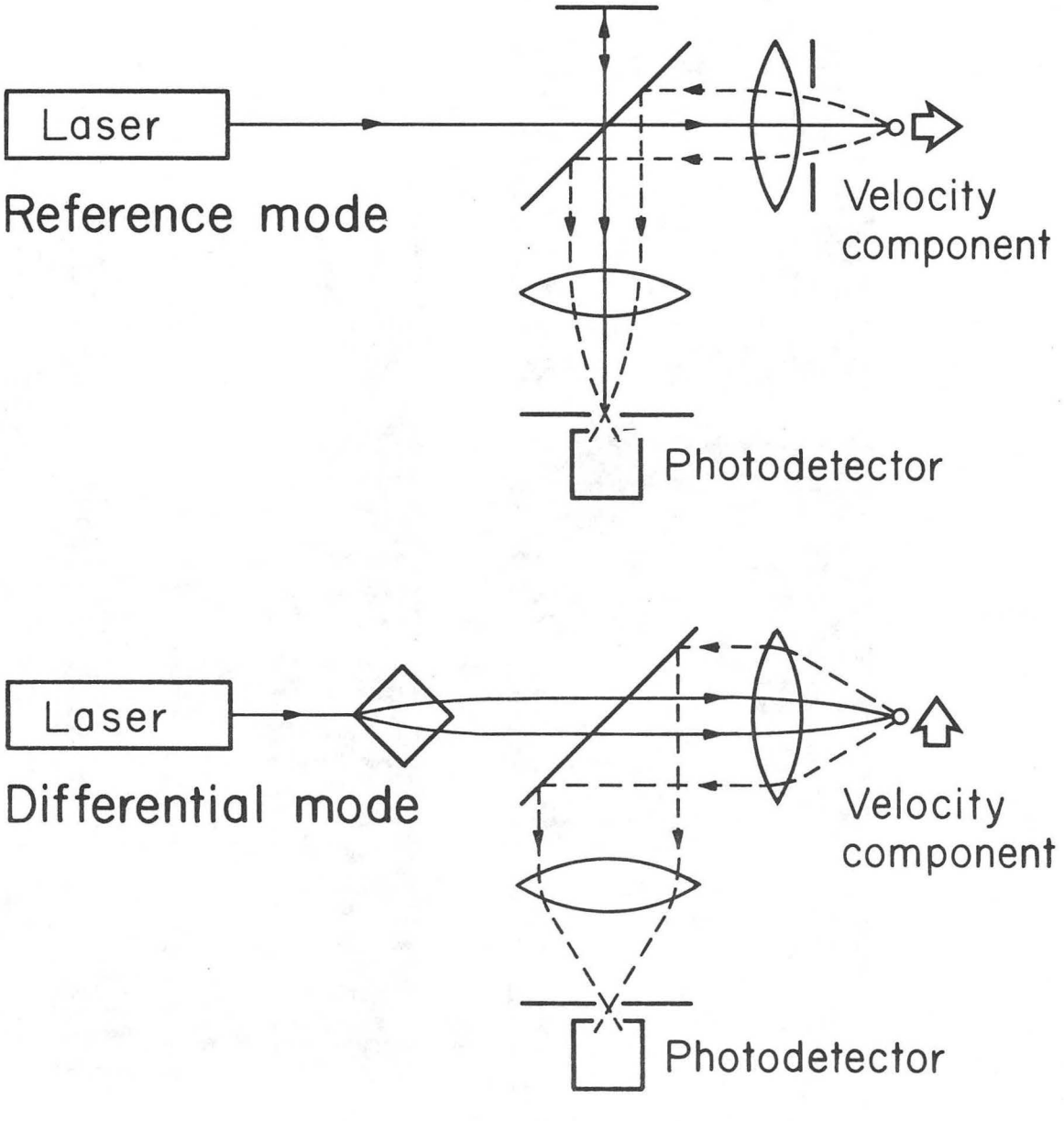
Laser
Reference mode
Velocity component
Photodetector
Laser
Differential mode
Velocity component
Photodetector
XBL 7410-4332A

Fig. 12

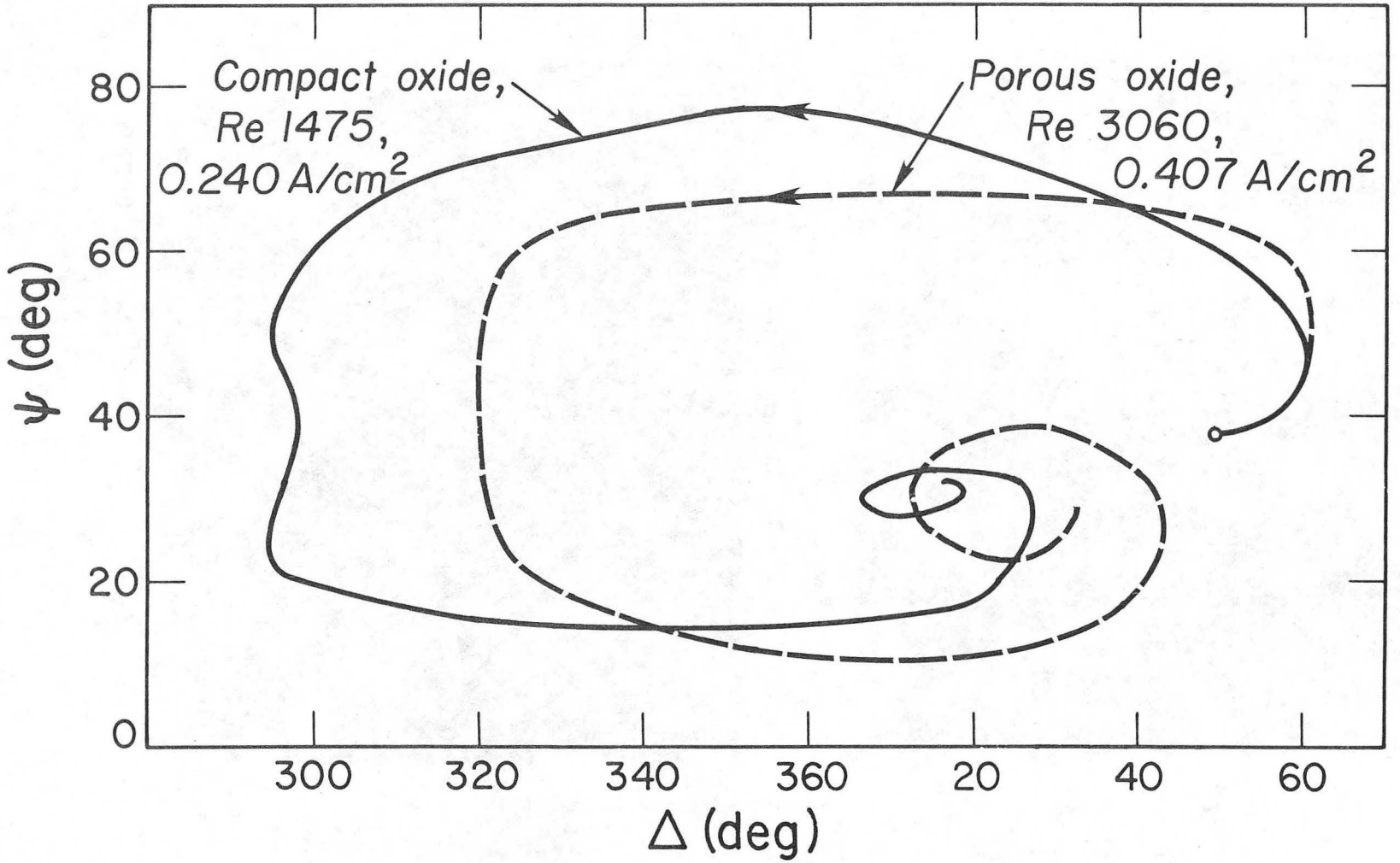


XBL 768-3877 A

Fig. 13.

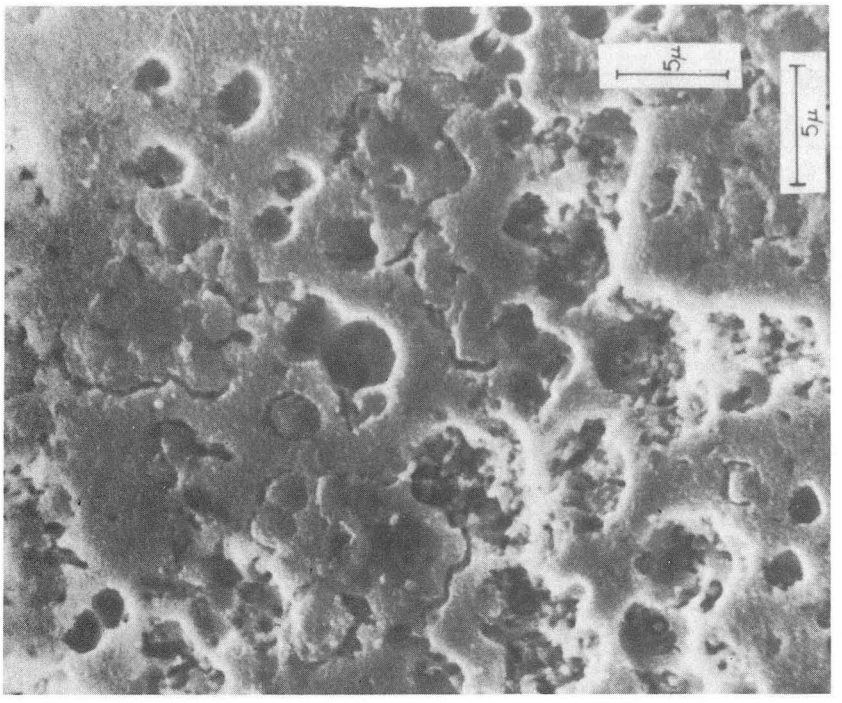


(b)

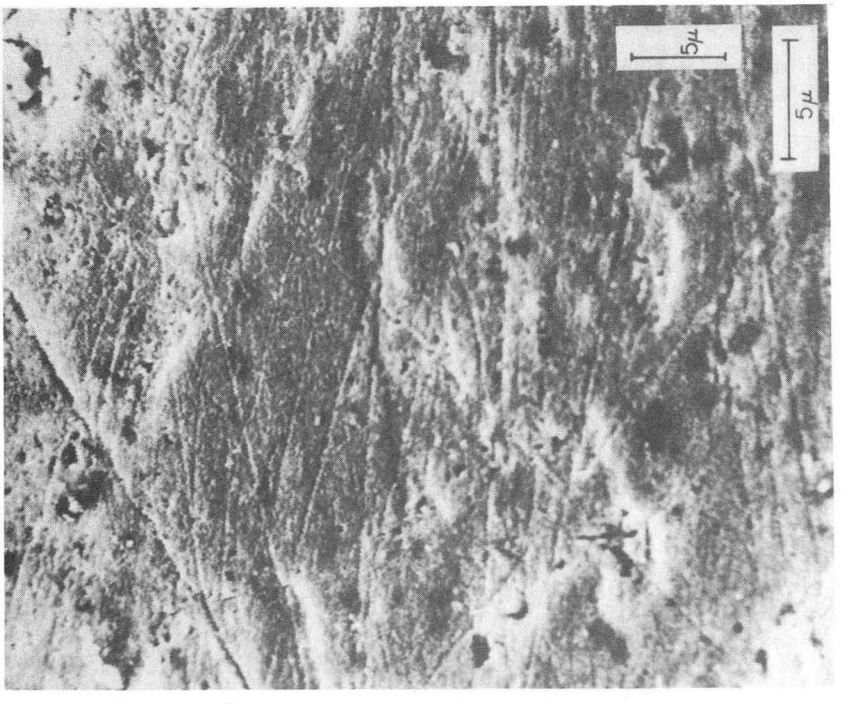


(a)

XBB 7410-7016A

Fig. 14.

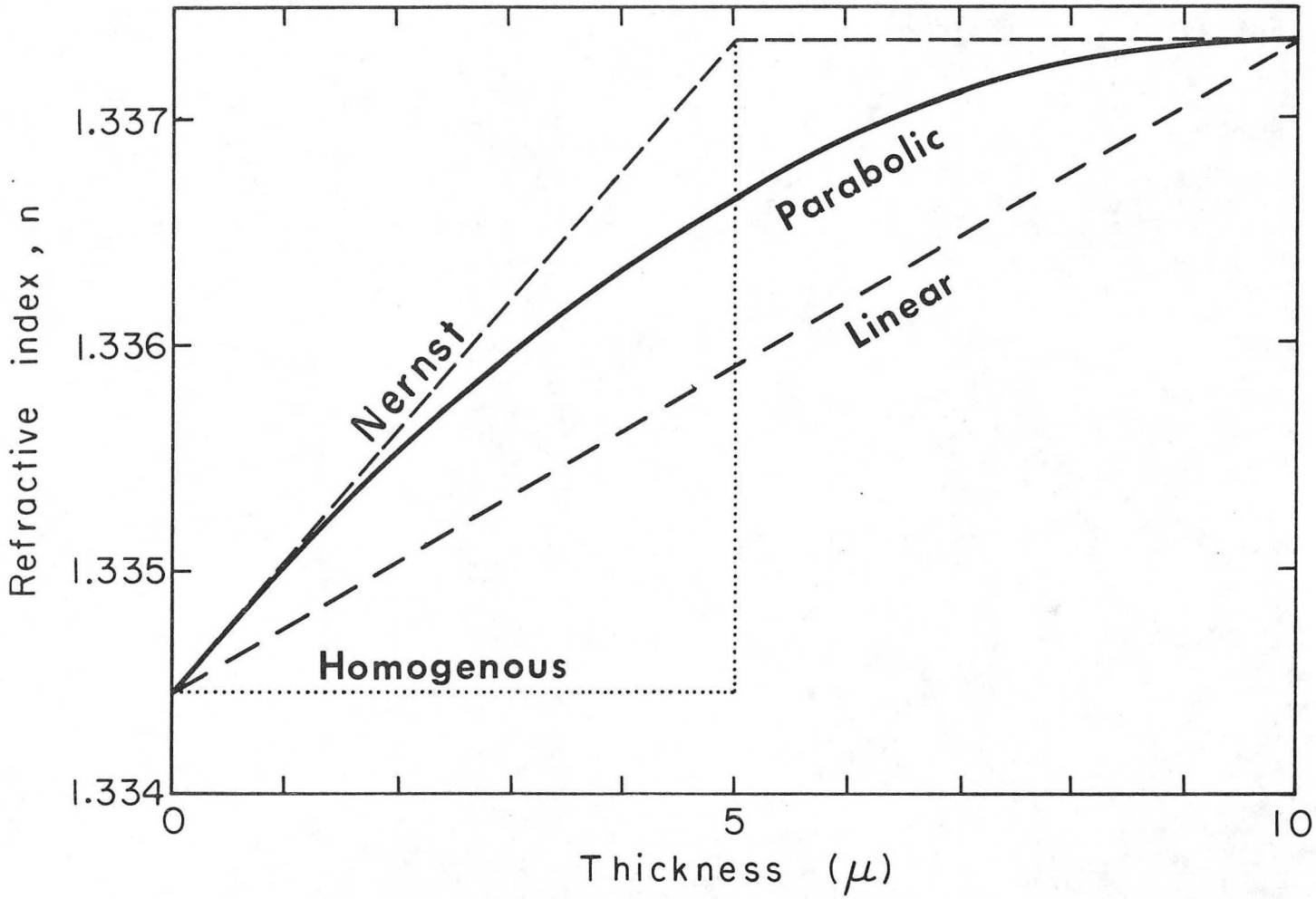


Fig. 15.

XBL768-3277A

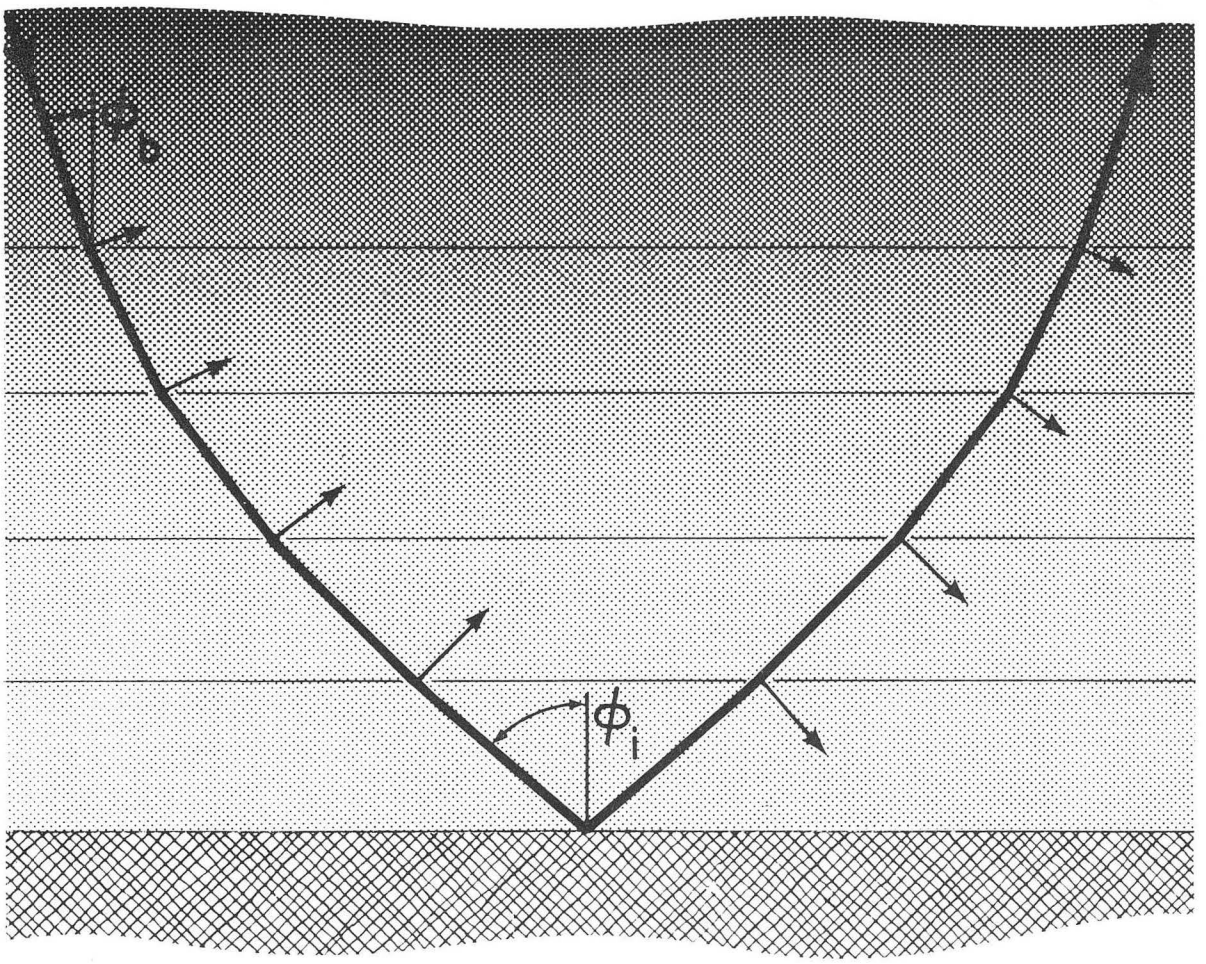


XBL7611-4369

Fig. 16.

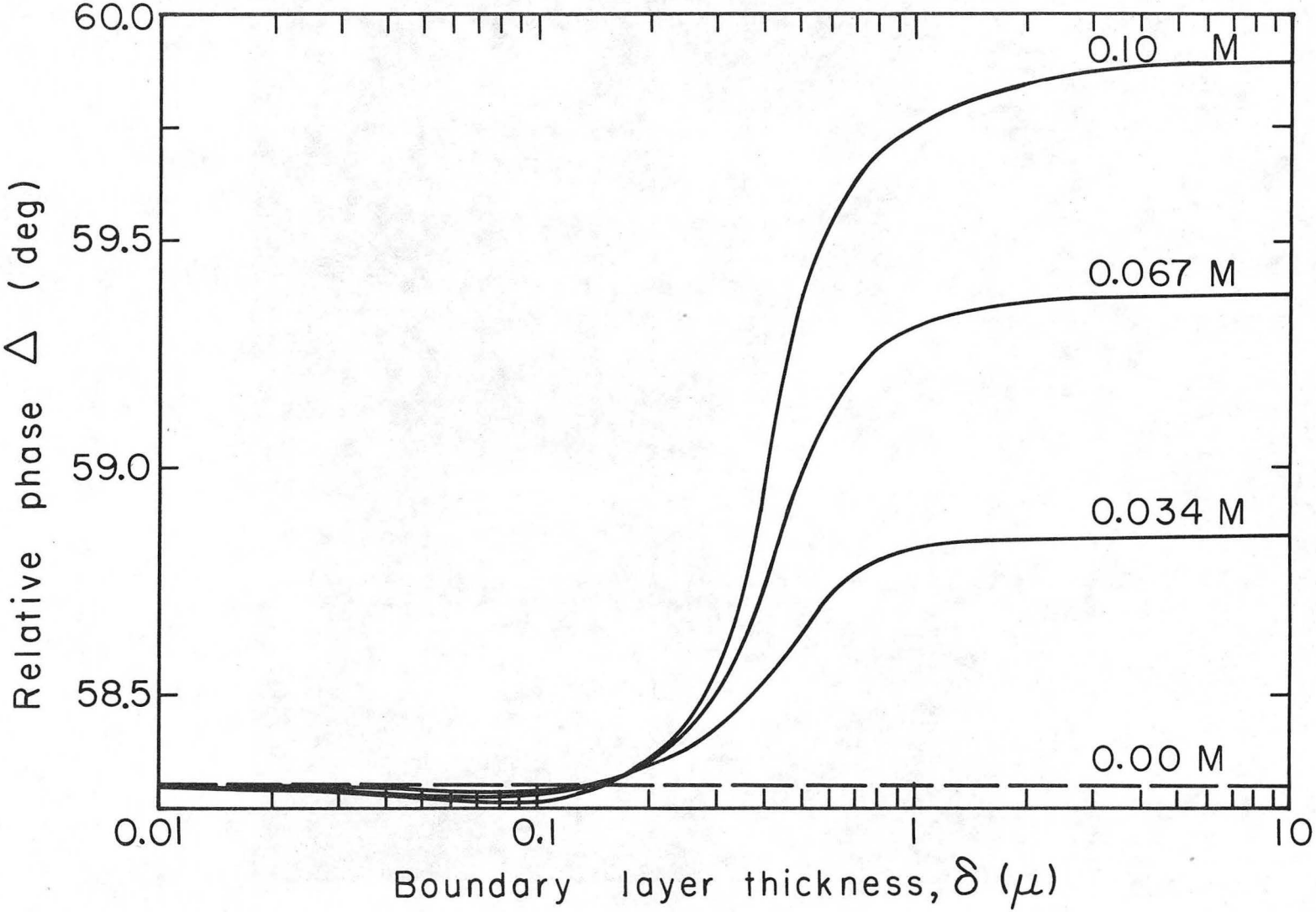


XBL755 – 2961

Fig. 17.

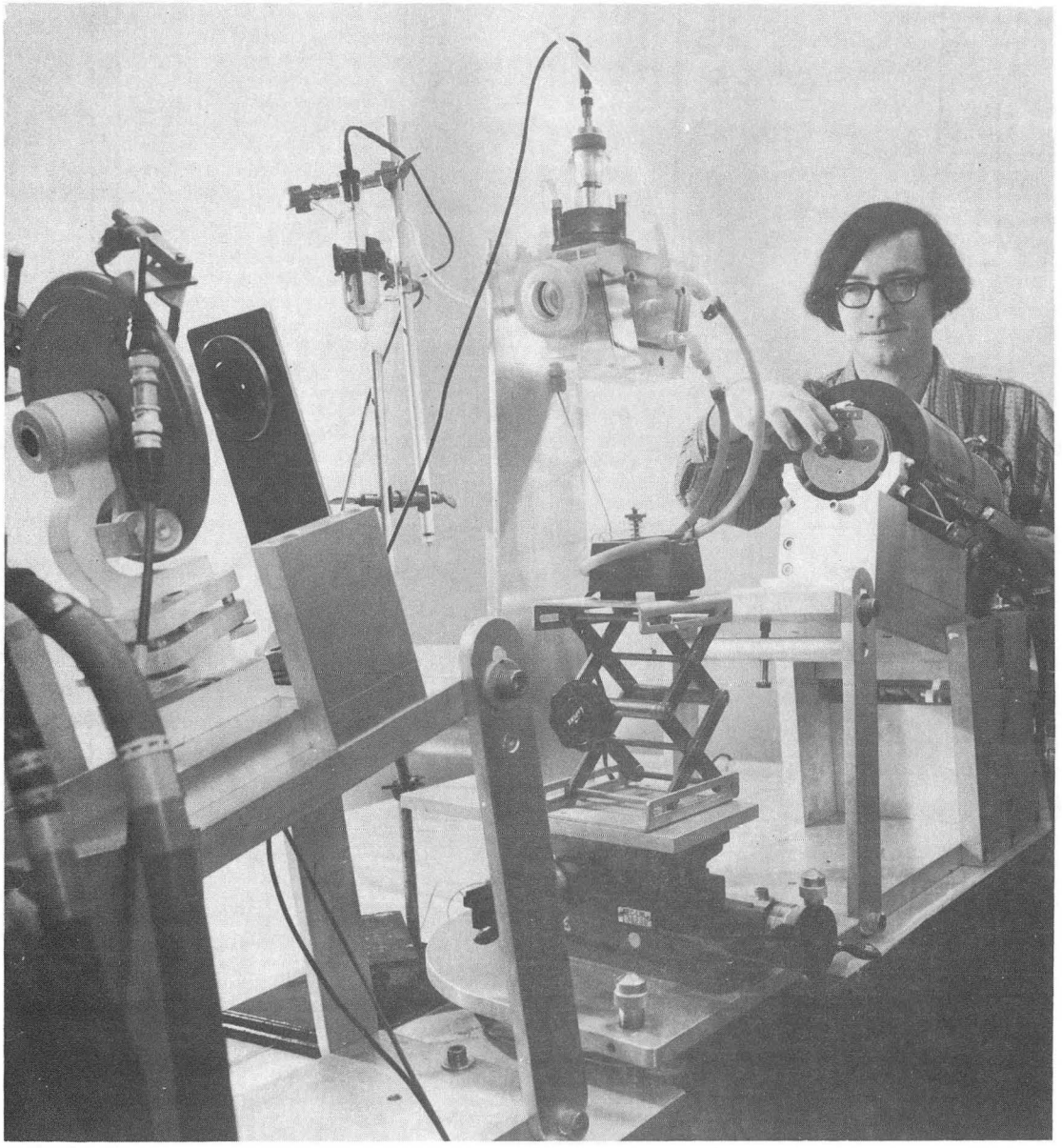

XBB 7510-7287

Fig. 18

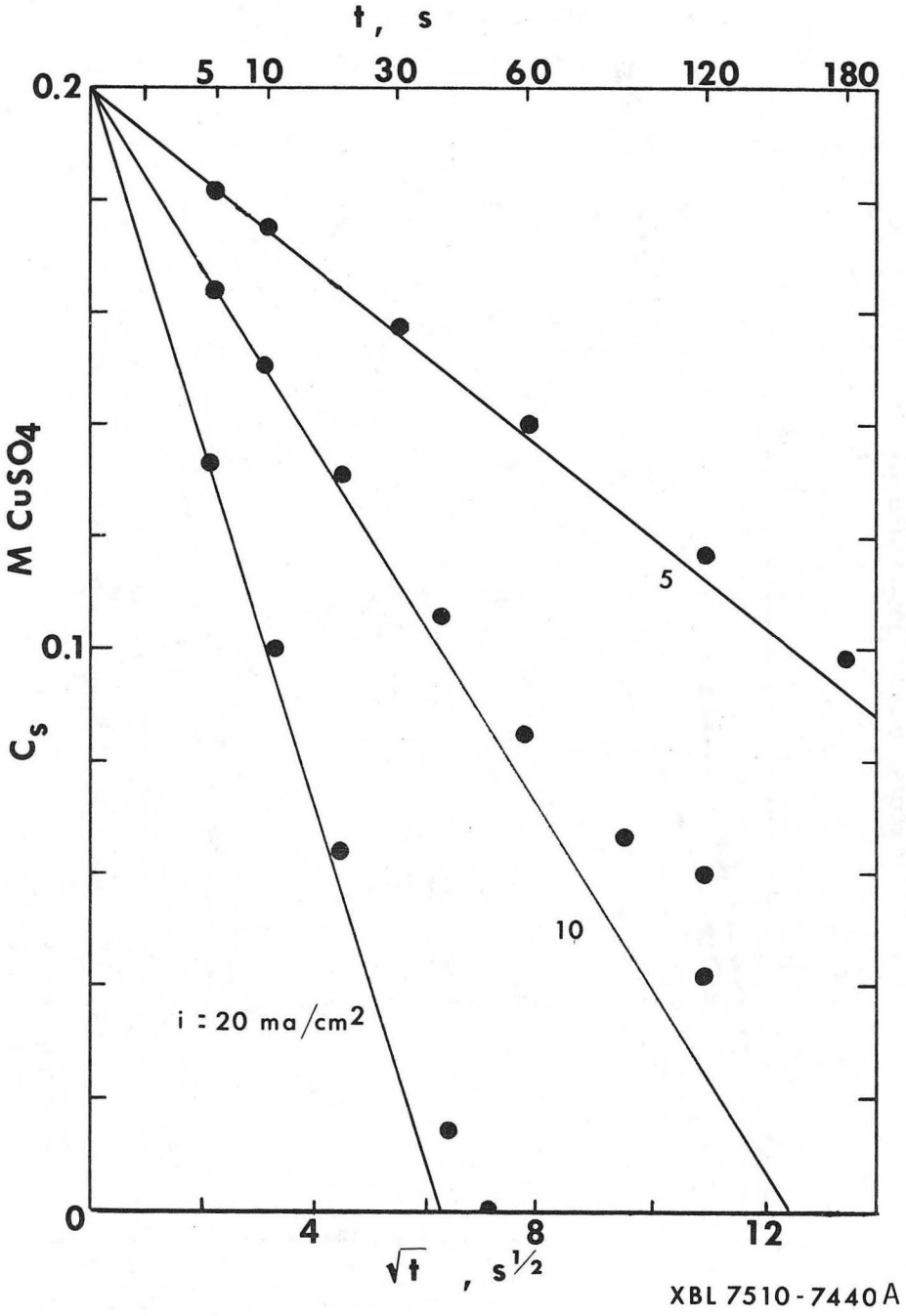


Fig. 19

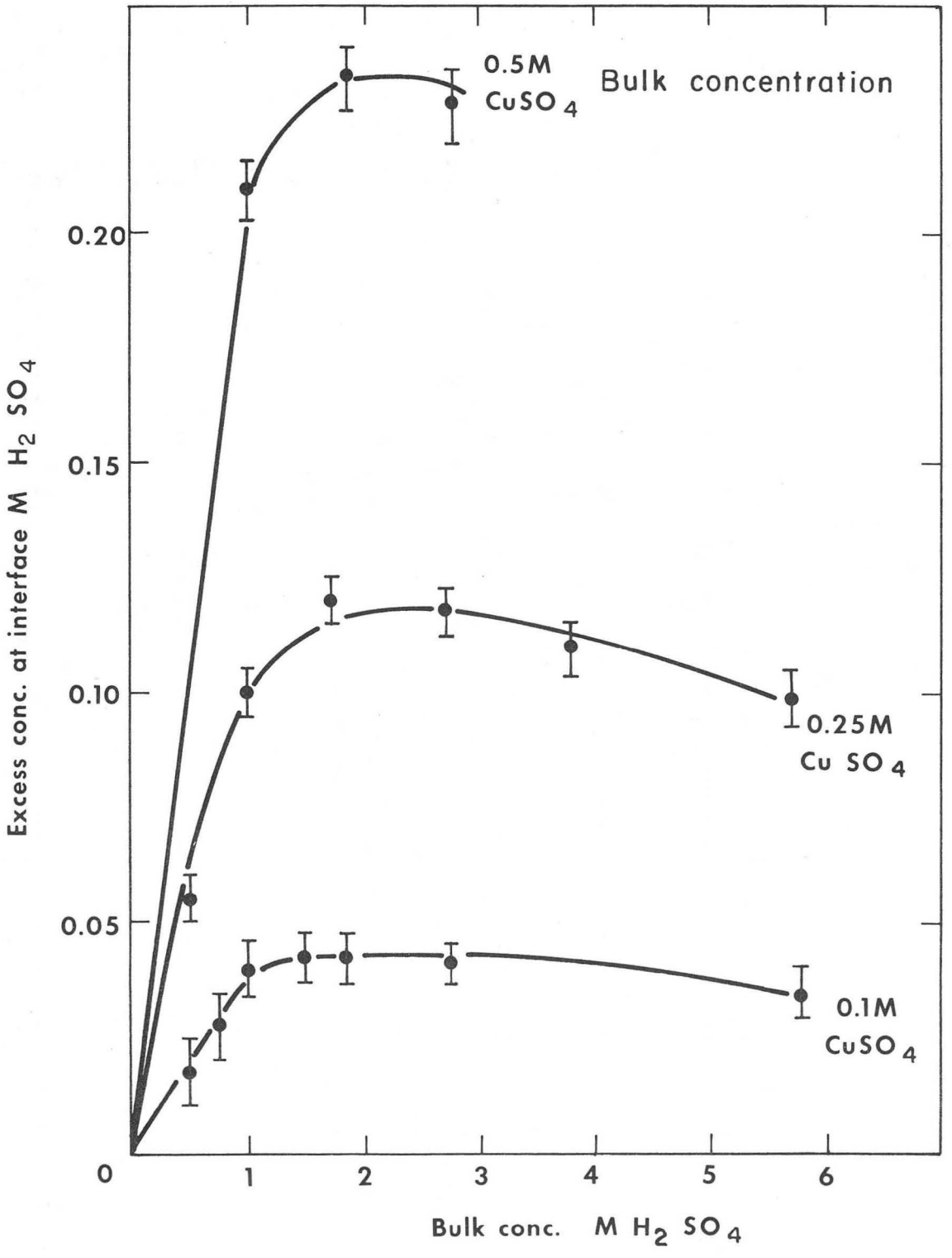


XBL 768-3276 A

Fig. 20

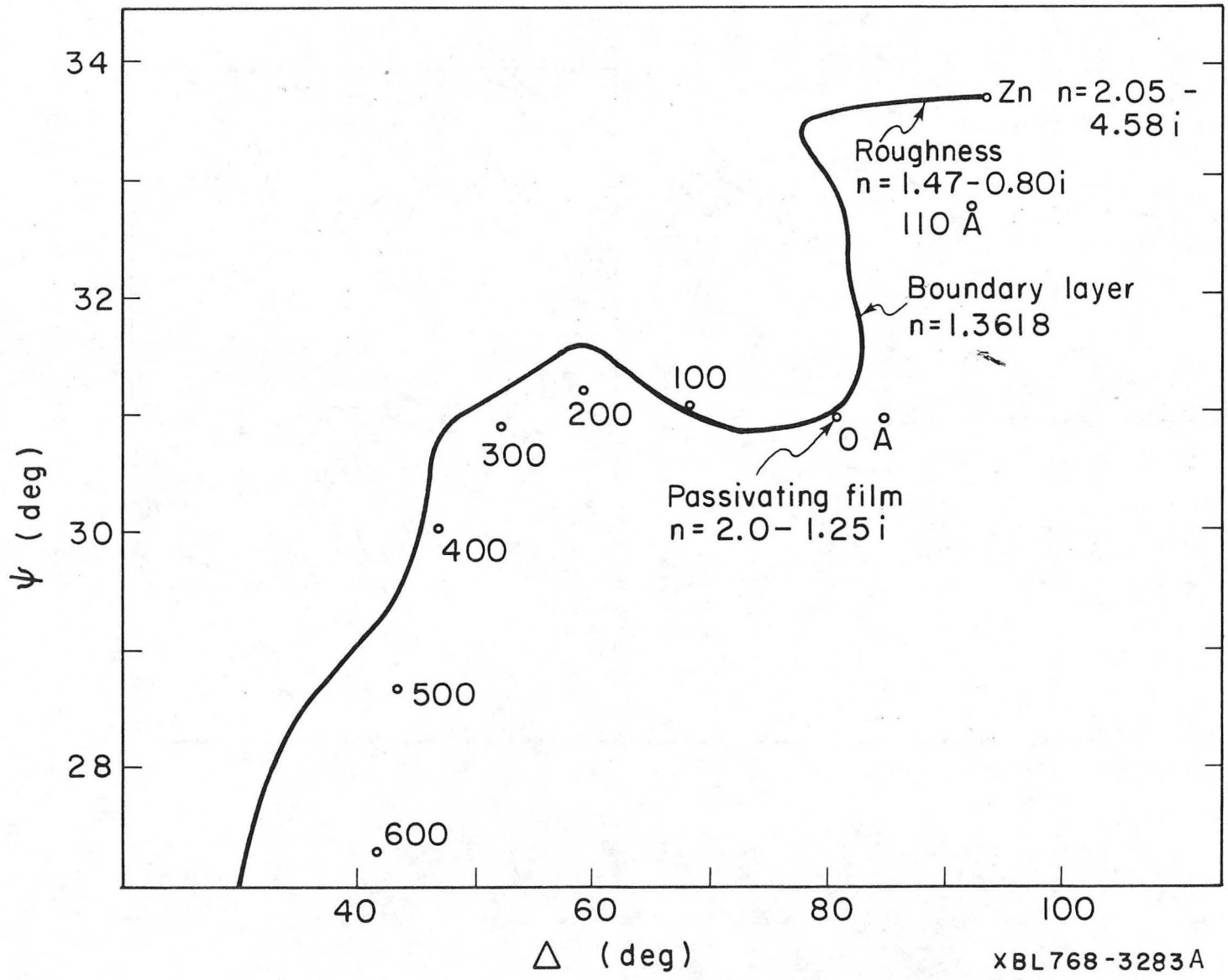


Fig. 21.

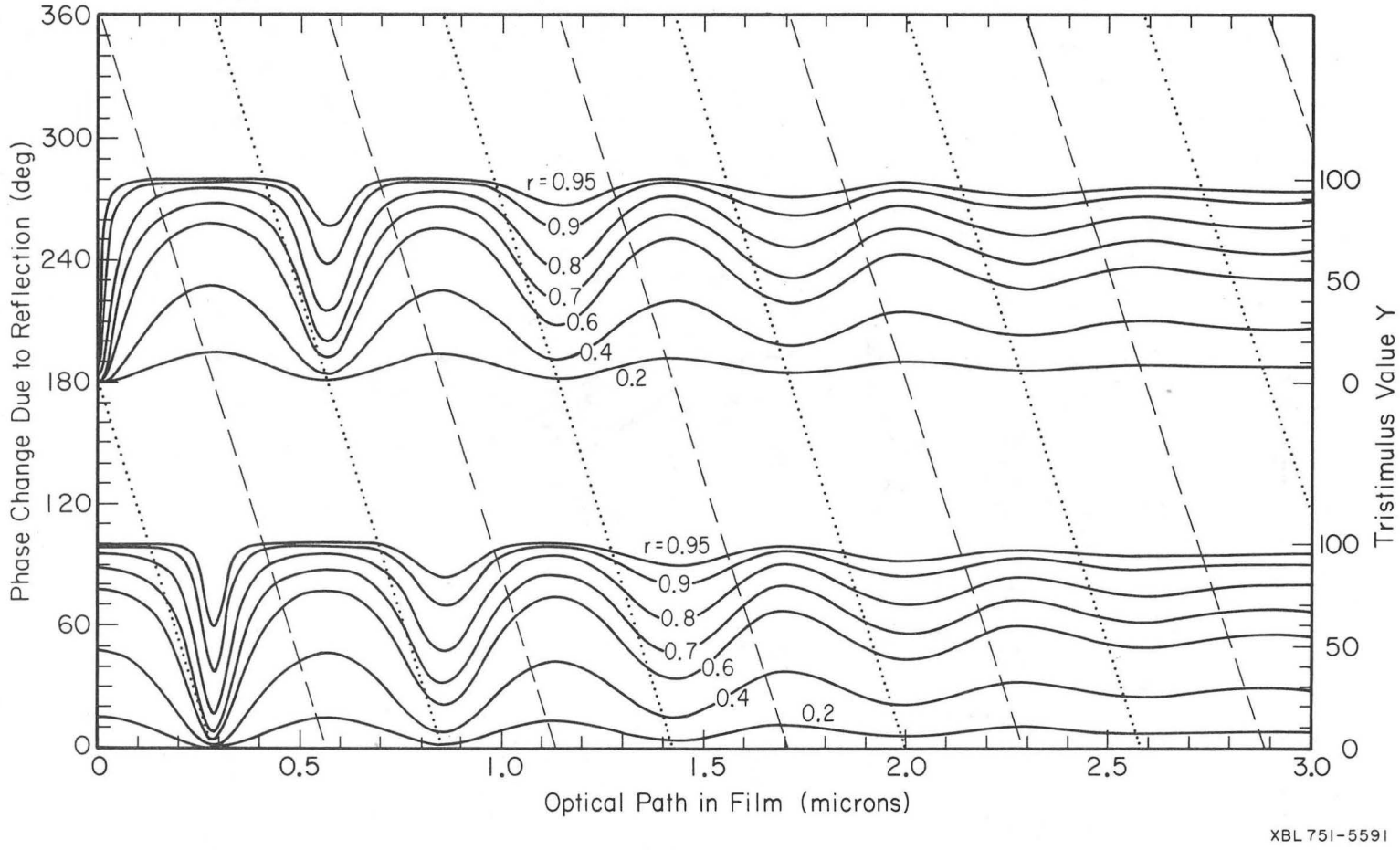
360
300
240
180
120
60
0
Phase Change Due to Reflection (deg)
r = 0.95
0.9
0.8
0.7
0.6
0.4
0.2
r = 0.95
0.9
0.8
0.7
0.6
0.4
0.2
100
50
0
100
50
0
Tristimulus Value Y
0
0.5
1.0
1.5
2.0
2.5
3.0
Optical Path in Film (microns)
XBL 751-5591

Fig. 22.

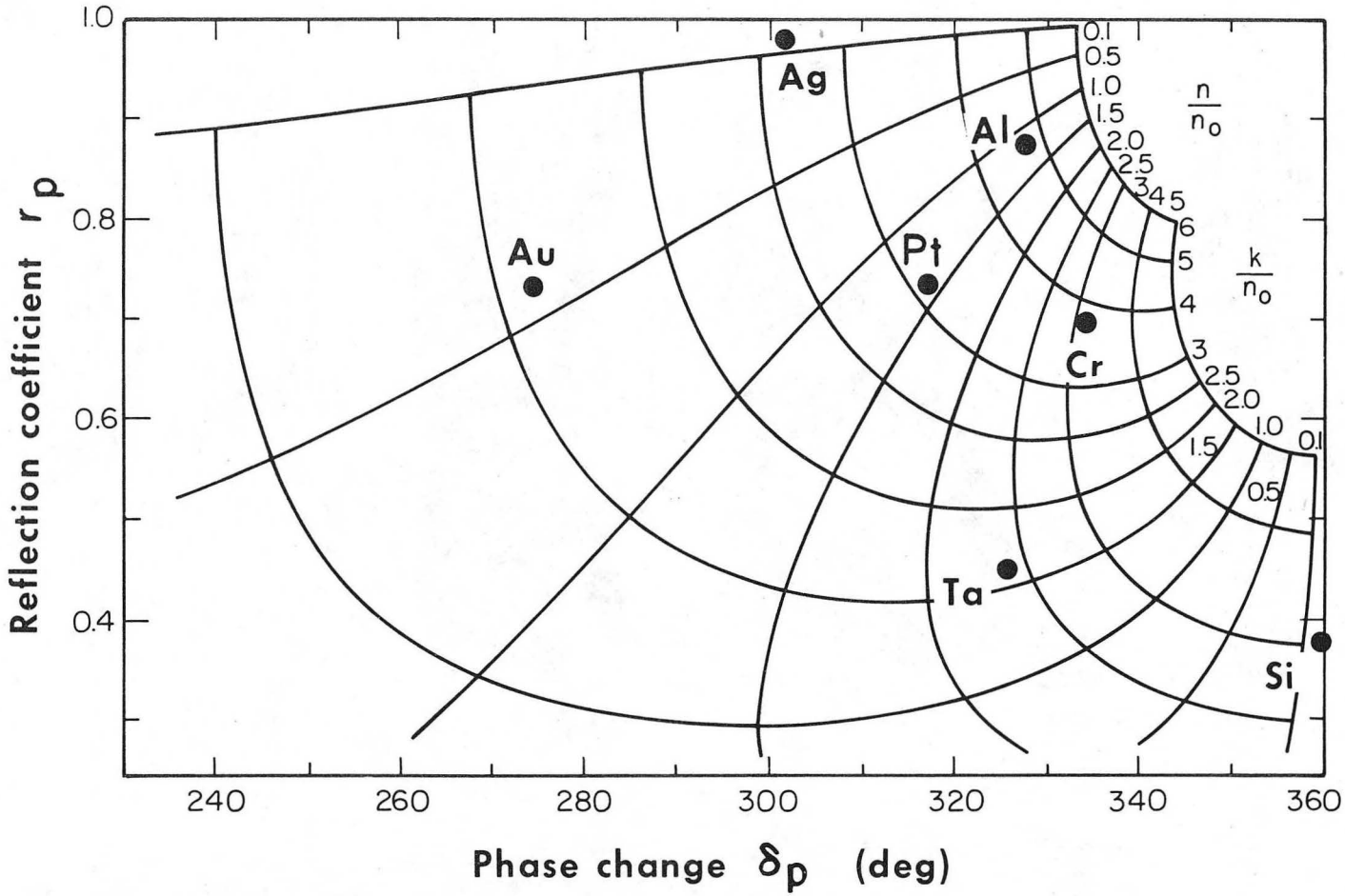


Fig. 23.

XBL768-3282 A

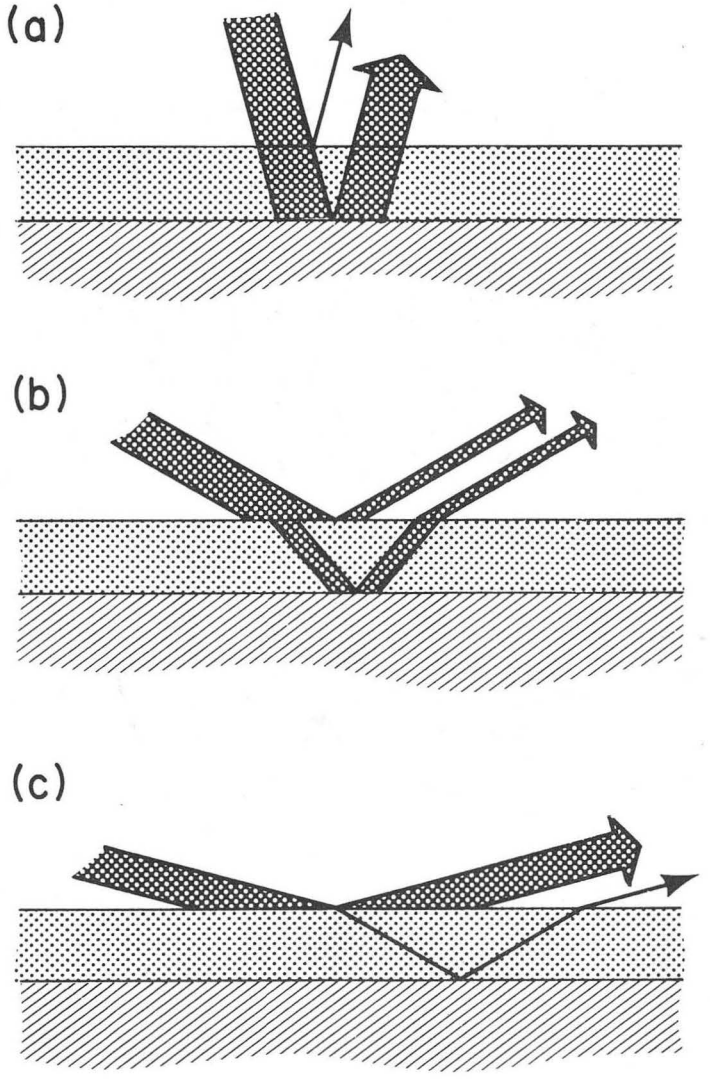


XBL7611-4370

Fig. 24

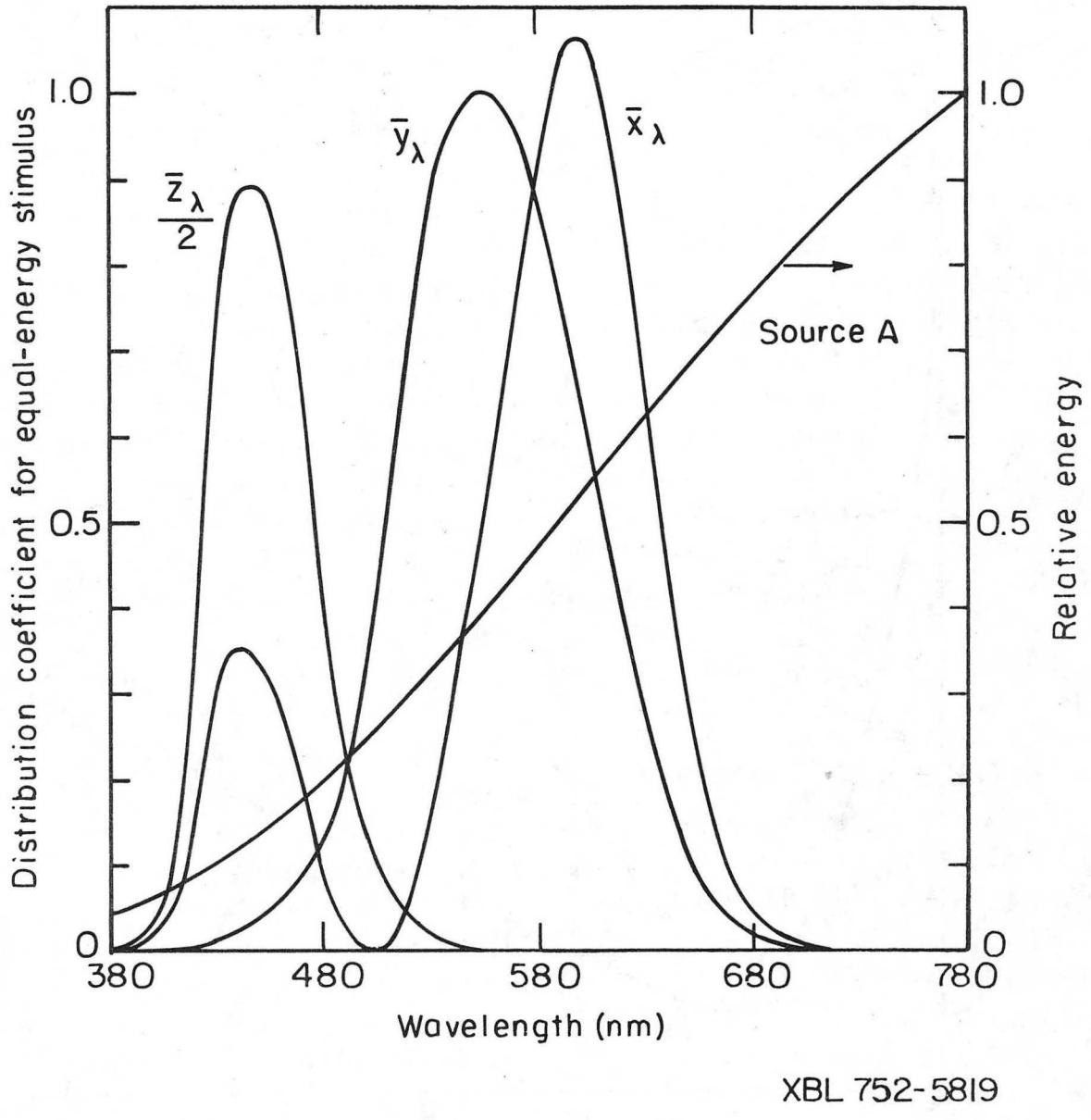


Fig. 25

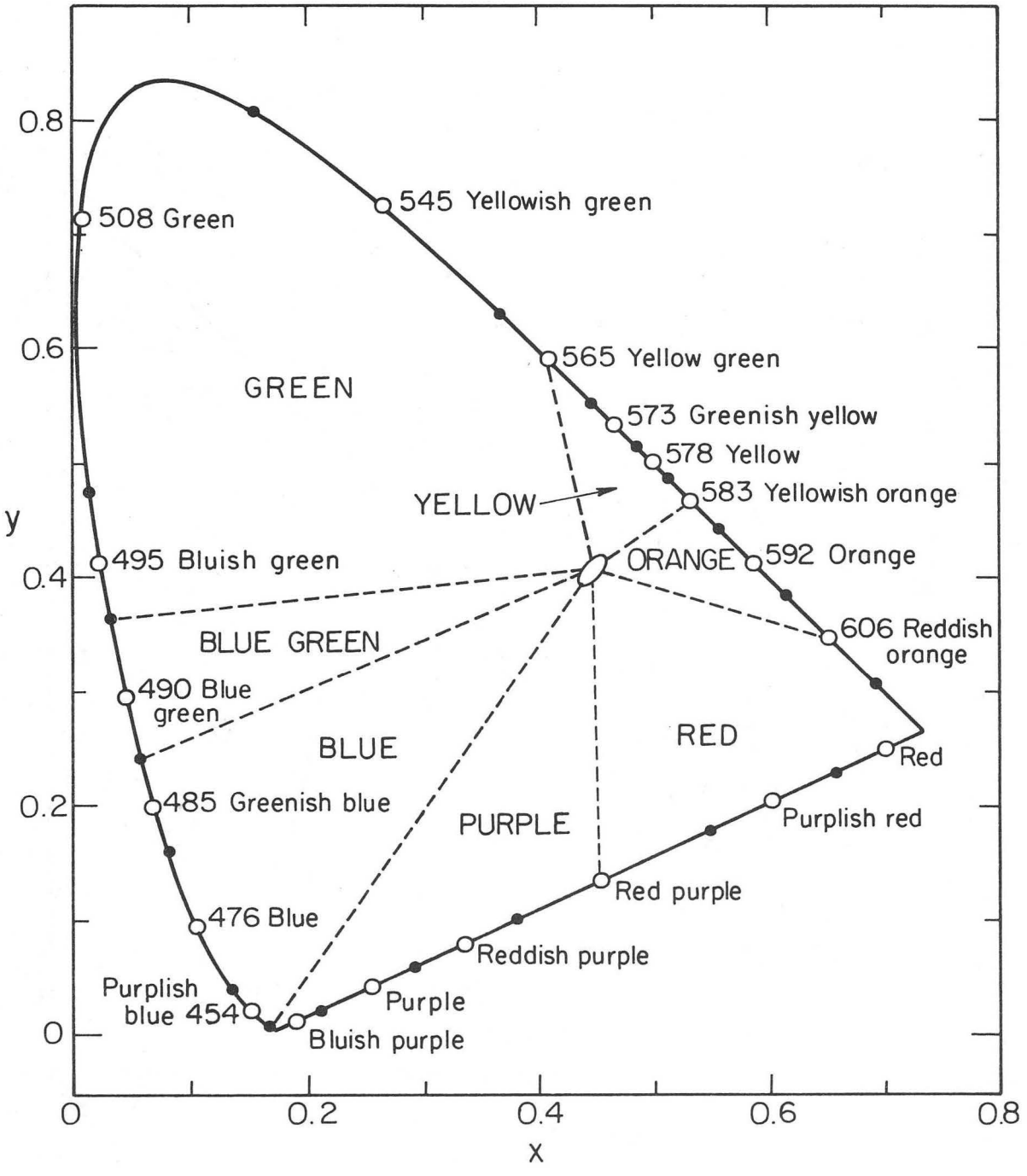
0.8
0.6
0.4
0.2
0
y
0
0.2
0.4
0.6
0.8
x
508 Green
545 Yellowish green
565 Yellow green
573 Greenish yellow
578 Yellow
583 Yellowish orange
592 Orange
606 Reddish orange
Red
Purplish red
Red purple
Reddish purple
Purple
Bluish purple
Purplish blue 454
476 Blue
485 Greenish blue
490 Blue green
495 Bluish green
GREEN
YELLOW
ORANGE
BLUE GREEN
BLUE
RED
PURPLE
XBL752-5824

Fig. 26

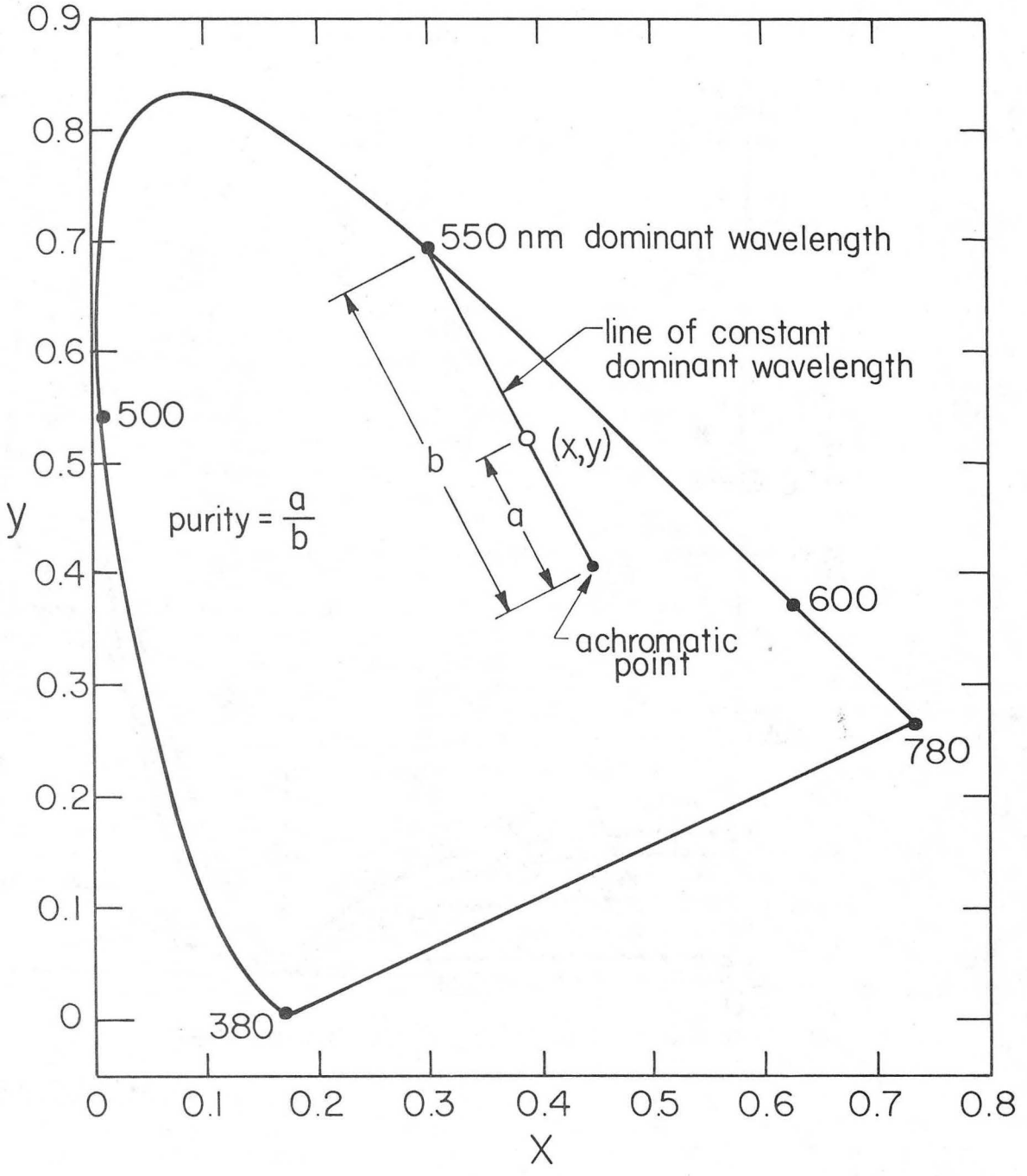


XBL 755-6355 A

Fig. 27

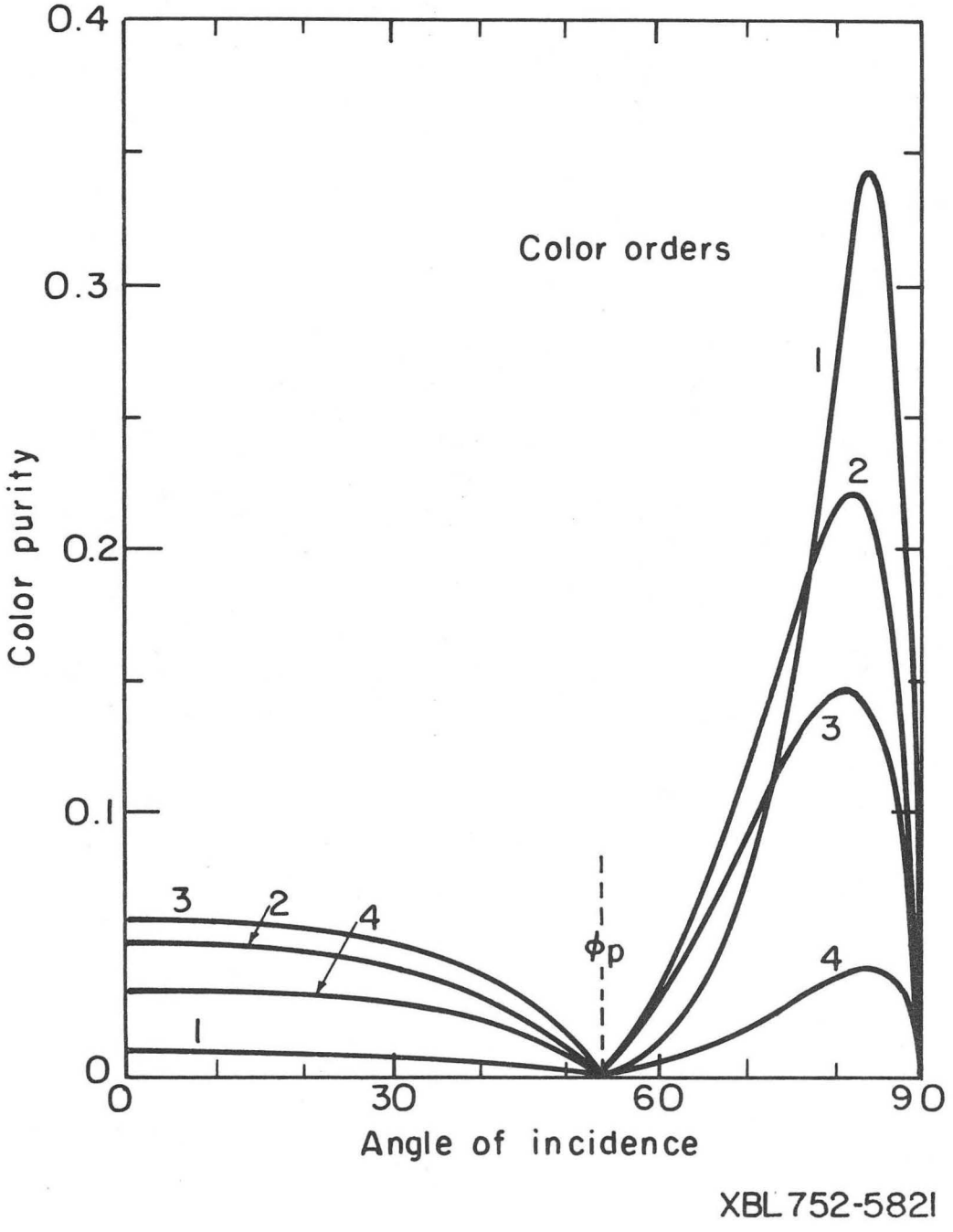
0.4
0.3
0.2
0.1
0
Color purity
Color orders
1
2
3
4
3
2
4
1
$\phi_p$
0
30
60
90
Angle of incidence
XBL752-5821

Fig. 28

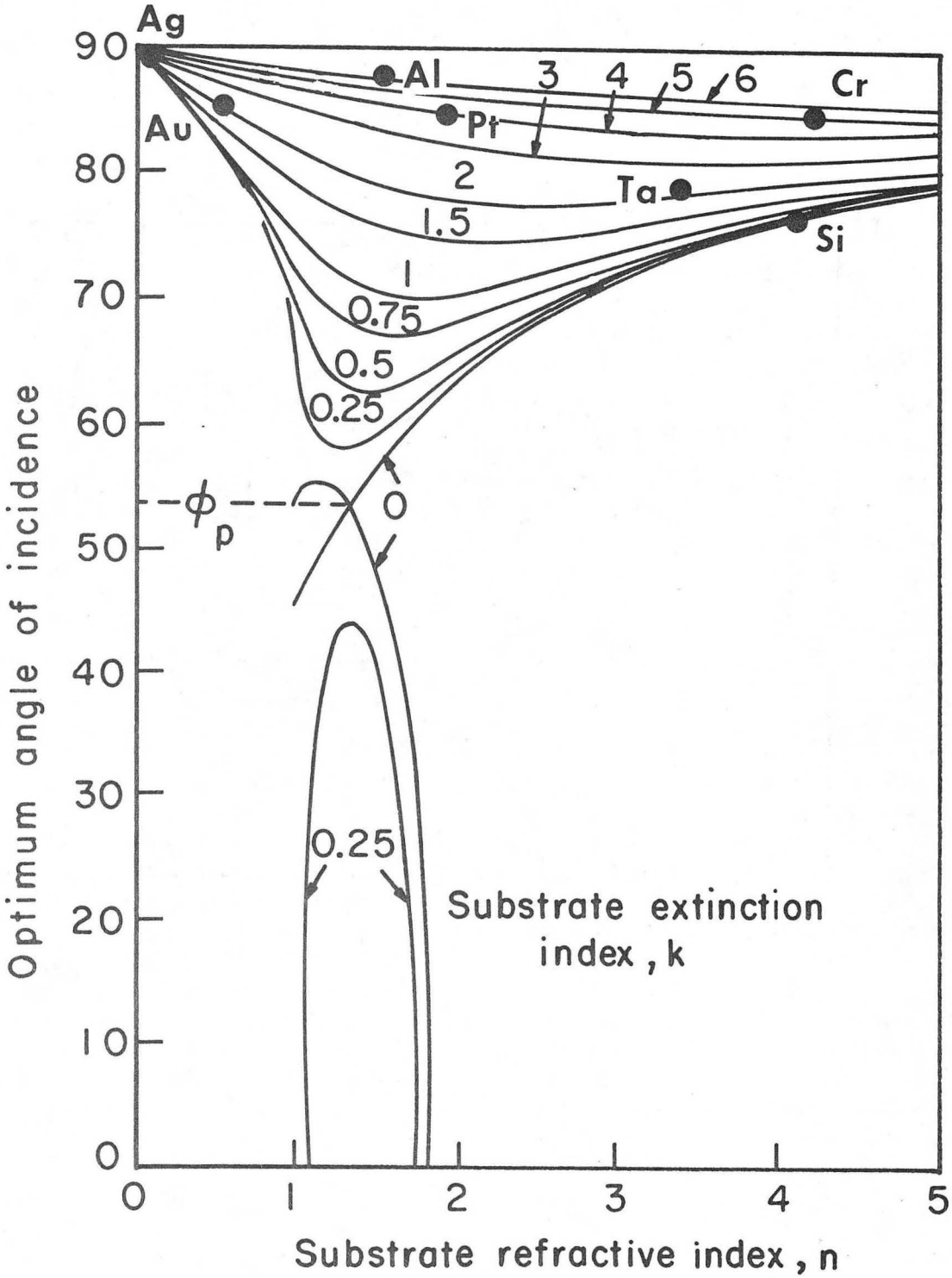


XBL768-3284A

Fig. 29

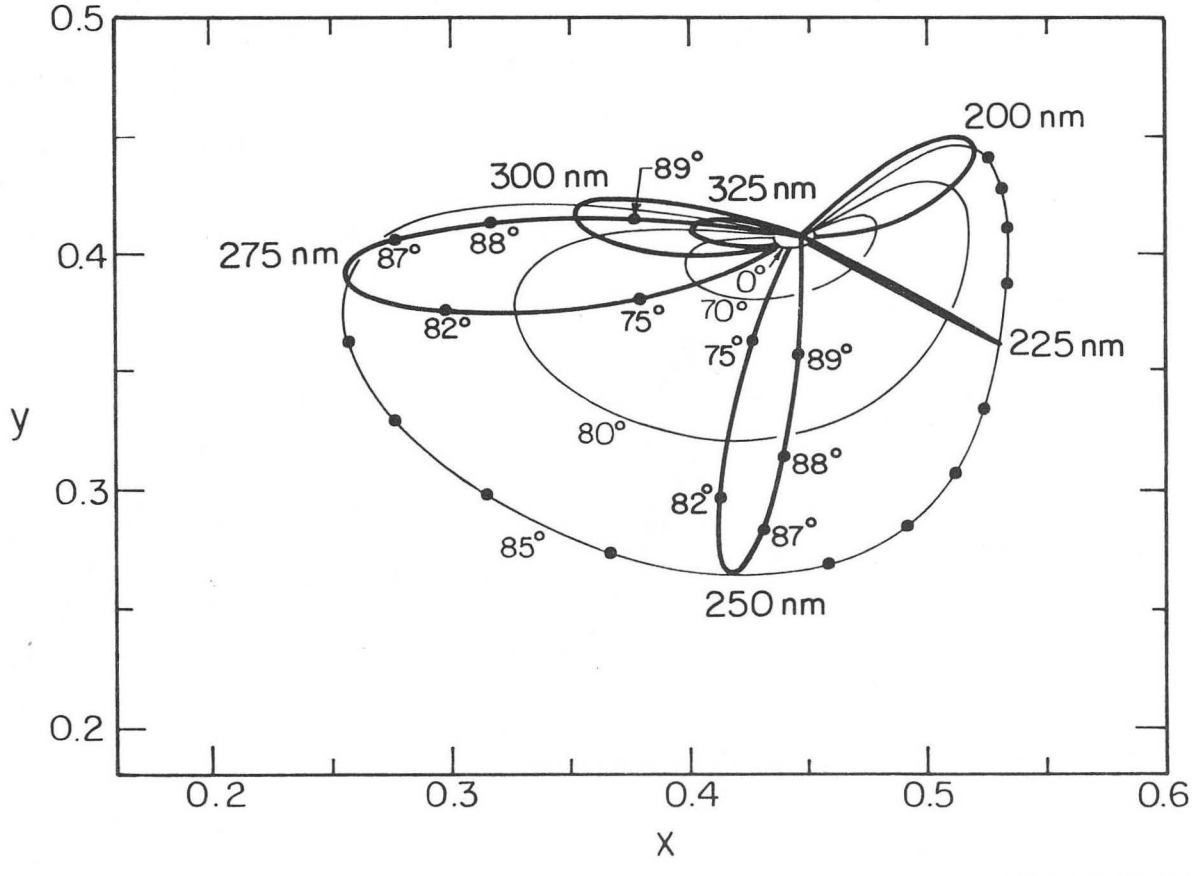


XBL752-5696

Fig. 30

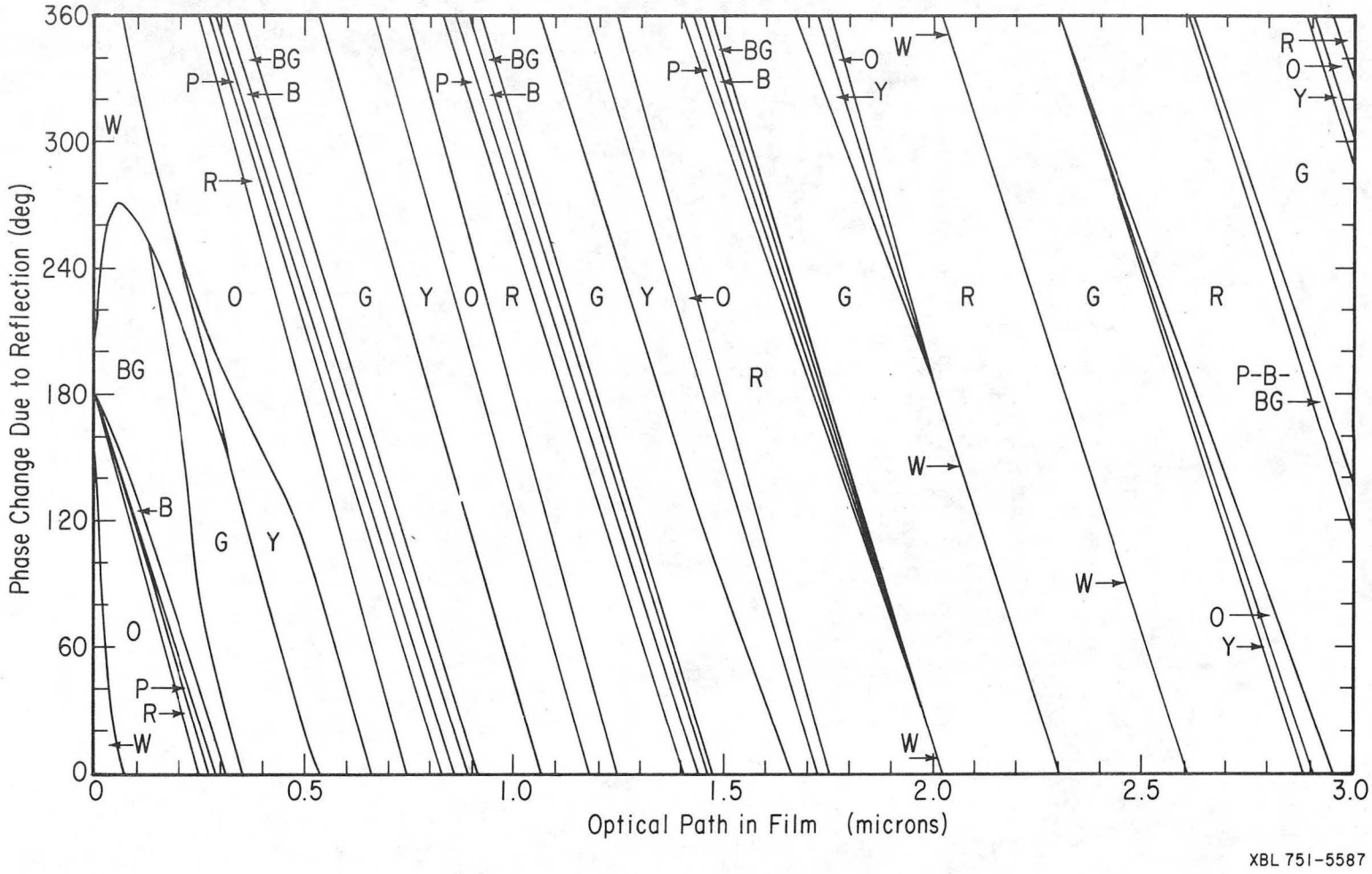


Fig. 31.

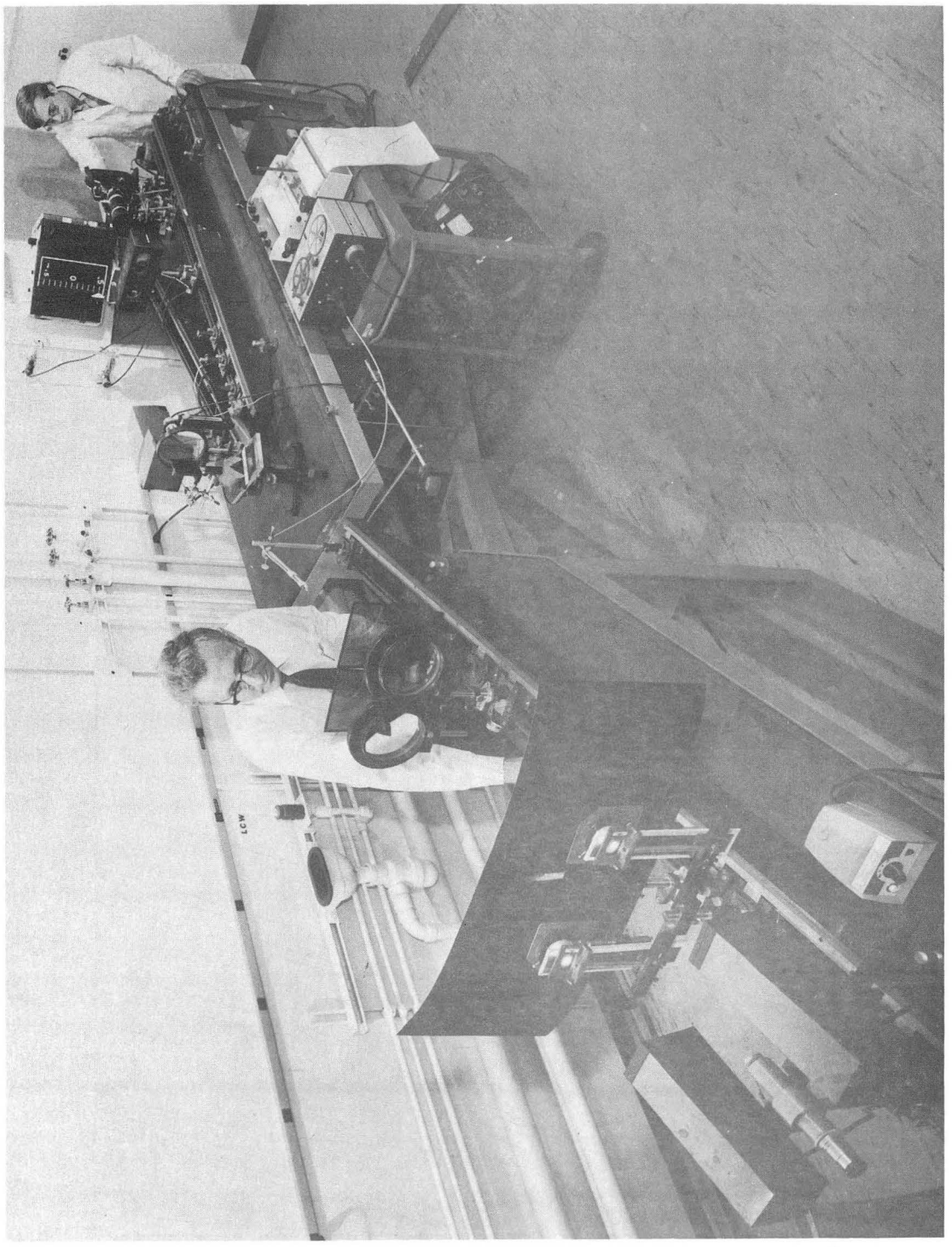

CBB 755-3842

Fig. 32

*TECHNICAL INFORMATION DIVISION*
*LAWRENCE BERKELEY LABORATORY*
*UNIVERSITY OF CALIFORNIA*
*BERKELEY, CALIFORNIA 94720*